

1 **Feasibility of improving a priori regional climate model**
2 **estimates of Greenland ice sheet surface mass loss**
3 **through assimilation of measured ice surface temperatures**

4 **M. Navari¹ S.A. Margulis¹, S.M. Bateni², M. Tedesco³, and P. Alexander^{3, 4},**
5 **Xavier Fettweis⁵**

6 [1]{Department of Civil and Environmental Engineering, University of California Los
7 Angeles, California}

8 [2]{Department of Civil and Environmental Engineering and Water Resources Research
9 Centre, University of Hawaii at Manoa, Hawaii}

10 [3]{Department of Earth and Atmospheric Sciences, City College of New York, New York,
11 New York}

12 [4]{Graduate Center of the City University of New York, New York, New York}

13 [5] {Department of Geography, University of Liège, Liège, Belgium}

14 Correspondence to: Mahdi Navari (navari@ucla.edu)

15

16 Submitted to: *The Cryosphere* on 04/20/2015

17

18

19

20

21

22

23

24

25

26

1

2 **Abstract**

3 The Greenland ice sheet (GrIS) has been the focus of climate studies due to its considerable
4 impact on sea level rise. Accurate estimates of surface mass fluxes would contribute to
5 understanding the cause of its recent changes and would help to better estimate the past,
6 current and future contribution of the GrIS to sea level rise. Though the estimates of the GrIS
7 surface mass fluxes have improved significantly over the last decade, there is still
8 considerable disparity between the results from different methodologies (e.g., Rae et al.,
9 2012; Vernon et al., 2013). Data assimilation approach can merge information from different
10 methodologies in a consistent way to improve the GrIS surface mass fluxes. In this study, an
11 Ensemble Batch Smoother data assimilation approach was developed to assess the feasibility
12 of generating a reanalysis estimate of the GrIS surface mass fluxes via integrating remotely
13 sensed ice surface temperature measurements with a regional climate model (a priori)
14 estimate. The performance of the proposed methodology for generating an improved posterior
15 estimate was investigated within an observing system simulation experiment (OSSE)
16 framework using synthetically generated ice surface temperature measurements. The results
17 showed that assimilation of ice surface temperature time series were able to overcome
18 uncertainties in near-surface meteorological forcing variables that drive the GrIS surface
19 processes. Our findings show that the proposed methodology is able to generate posterior
20 reanalysis estimates of the surface mass fluxes that are in good agreement with the synthetic
21 true estimates. The results also showed that the proposed data assimilation framework
22 improves the root-mean-square-error (RMSE) of the posterior estimates of runoff,
23 sublimation/evaporation, surface condensation and surface mass loss fluxes by 61%, 64%,
24 76%, and 62% respectively over the nominal a priori climate model estimates.

25

1 **1 Introduction and Background**

2 The Greenland ice sheet (GrIS) has recently experienced thinning of the marginal ice (e.g.
3 Straneo et al. 2013, Khan et al., 2014), thickening of its interior (e.g. Johannessen et al., 2005;
4 Fettweis, 2007), acceleration and increase in ice discharge from many of Greenland’s outlet
5 glaciers (e.g. Rignot et al., 2008; Wouters et al., 2013), and enhanced surface melt (e.g.
6 Tedesco et al., 2013; Vernon et al., 2013). The melting of the GrIS due to increased
7 temperature has the potential to affect deep ocean circulation, and sea level rise (Hanna et al.,
8 2005; Fettweis et al., 2007; Tedesco 2007, Rahmstorf et al., 2015). Van Angelen et al. (2012)
9 and Fettweis et al. (2013) predict that meltwater runoff will be the dominant mass loss process
10 in the future due to the retreat of the tidewater glaciers above sea level; a recent study
11 showing that the dynamic mass loss was reduced from 58% before 2005 to 32% for the period
12 between 2009 and 2012 (Enderlin et al., 2014).

13 Many studies (e.g. van de Wal et al., 2012) have taken advantage of in situ measurements to
14 provide a direct point-scale estimate of the surface mass balance (SMB, i.e. the difference
15 between accumulation and ablation). However, with these limited in situ measurements alone,
16 large-scale mapping of the GrIS surface mass fluxes (i.e. precipitation, evaporation,
17 sublimation, condensation, and runoff) is impossible. The availability of remote sensing data
18 and/or products has taken GrIS from a remote “data poor” region that is reliant mostly on
19 sparse in situ measurements to a potentially “data rich” environment. In this regard, a key
20 research objective is to better understand how such data can be optimally leveraged for
21 quantitatively estimating the surface mass balance (SMB) and its associated fluxes.

22 Surface remote sensing data and products (i.e., surface or skin temperature, multi-frequency
23 brightness temperature, and albedo) have been used to characterize various aspects of SMB
24 such as snow melt, melt extent, melt duration, new snow, extreme melt events (e.g. Abdalati
25 and Steffen, 1995; Tedesco et al., 2011; Box et al., 2012; Hall et al., 2013). However, the
26 relationship between surface remote sensing data/products and surface mass fluxes are most
27 often indirect and implicit. For example, ice surface temperature can be indicative of melt, but
28 it fails to quantitatively estimate the volume of meltwater produced. More importantly, other
29 surface mass fluxes such as evaporation, condensation, sublimation, and runoff cannot be
30 directly quantified via remote sensing. This makes the possibility of quantitatively
31 characterizing the surface mass fluxes from remote sensing retrieval algorithms difficult if not
32 impossible. It can therefore be argued that the information content of remotely sensed data

1 remains underutilized due to indirect and implicit links between the various data streams and
2 surface mass fluxes.

3 Given the limitations of the observation-based methods, numerical models offer an alternative
4 mechanism to quantify the GrIS surface mass fluxes. Several model-based approaches have
5 been used to characterize the spatio-temporal variability of the GrIS surface mass fluxes in
6 both historical and future contexts (e.g. Hanna et al., 2011,2013; Box et al., 2006; Fettweis,
7 2011; Ettema et. al., 2009; Lewis and Smith, 2009; Vernon et al. 2013; Franco et al. 2013).
8 Although the aforementioned methodologies have provided the ability to estimate the GrIS
9 SMB and related fluxes, their estimates vary considerably, mainly due to the different physics
10 parameterizations in the models and simplifying assumptions, the inherent uncertainty of each
11 method, error in model and input data, and the length of data records (e.g. Rignot et al., 2011;
12 Vernon et al., 2013; Smith et al., 2015). Therefore, it is imperative to design techniques that
13 bridge the gap between different methods by merging relevant data streams with a physical
14 model with the aim of better spatial-temporal characterization of the GrIS surface mass
15 fluxes. In this study, we provide an example of taking advantage of information in the
16 relevant data streams to provide a better spatial-temporal characterization of the model
17 outputs (i.e., the GrIS surface mass fluxes). This can be done using a data assimilation
18 approach which attempts to merge model estimates with measurements in an optimal way
19 (Evensen, 2009).”

20

21 **2 Motivation and science questions**

22 To date, to the best of the authors’ knowledge, there have been no attempts at merging surface
23 remote sensing data with models using a data assimilation (DA) framework to fully resolve
24 and quantify estimates of the GrIS surface mass fluxes. Data assimilation techniques have
25 been heavily used in hydrology to estimate soil moisture (e.g. Reichle et al., 2002; Margulis et
26 al., 2002; Al-Yaari et al., 2014), predict snow water equivalent (SWE) (e.g. Durand et al.,
27 2008; De Lannoy et al., 2012; Giroto et al., 2014a; Zhang et al., 2014), estimate runoff (e.g.
28 Crow and Ryn 2009; Franz et al., 2014), improve estimates of radiative fluxes (e.g. Forman
29 and Margulis 2010; Xu et al., 2011), and characterize snowpack properties and freeze-thaw
30 state of the underlying soil (Bateni et al., 2013, 2015). DA so far has been underutilized in
31 applications aimed at characterizing GrIS dynamics. Recently, Goldberg and Heimbach
32 (2013), and Morlighem et al. (2013) used variational DA methods to characterize the interior

1 and basal properties of ice sheets and ice shelves. Larour et al. (2014) assimilated surface
2 altimetry data into the reconstructions of transient ice flow dynamics to infer basal friction
3 and surface mass balance of the northeast Greenland ice stream. However, the use of DA for
4 estimating GrIS SMB terms remains relatively unexplored. Assessing the feasibility of such
5 approaches in providing a mechanism for improving quantitative estimates of SMB is the key
6 motivation of this work.

7 This study utilizes an observing system simulation experiment (OSSE) framework to assess
8 the feasibility of the proposed DA system. The OSSE framework uses synthetically generated
9 ice surface temperature (IST) measurements consistent with a “true” realization of SMB
10 evolution. This study addresses the following science questions: 1) Can assimilation of IST
11 measurements overcome errors and uncertainties in the near-surface meteorological forcing
12 variables for snow/ice modelling? 2) Can a DA framework be used to reduce the uncertainty
13 and/or correct biases in a priori estimates of surface mass fluxes from a regional climate
14 model?

15 This paper is arranged as follows: Sect. 3 contains the description of the models and methods
16 used in this work. The experimental design is given in Sect. 4. The results and evaluation of
17 the proposed methodology are discussed in Sect. 5. Finally, key conclusions and future
18 research directions are reported in Sect. 6.

19

20 **3 Models and Methods**

21 **3.1 Study domain**

22 The study domain covers the entire GrIS, which is discretized with a grid size of 25 km by 25
23 km to match the domain used in the regional atmospheric model described below. The focus
24 is on fully snow/ice covered pixels. Figure 1 shows the different GrIS mass balance zones
25 based on a forward simulation for the year 2010. The ablation zone is defined as the region of
26 the GrIS where the annual surface mass balance is negative. The dry snow zone is defined as
27 the region where the mean annual temperature is less than -25°C (Cuffey and Paterson 2010)
28 and melt generally does not occur. The area between the ablation zone and the dry snow zone
29 is considered the percolation zone where surface meltwater percolates downward into the
30 snow layers. It should be noted that the digital elevation model (DEM) over the ice sheet

1 originates from a high-resolution map generated by Bamber et al. (2001). The elevation of the
2 ice sheet increases from almost zero in the coastal regions up to about 3400 m at the summit.

3 **3.2 Data**

4 Surface temperature plays an important role in the coupled GrIS surface energy and surface
5 mass budget. It is the key factor that regulates partitioning of net radiation into the subsurface
6 snow/ice, sensible and latent heat fluxes. Surface temperature also influences the generation
7 of runoff, the temperature profile evolution, and even basal melt (Hall et al., 2013). Space-
8 borne instruments can provide estimates of IST. The retrieved IST is directly related to snow
9 surface emissivity (Hook et al., 2007). The emissivity of the snow surface is a function of
10 grain size and liquid water content, which both are under the influence of surface processes
11 (Hall et al., 2009). These facts support the idea that clear-sky IST, of all remote sensing
12 products available, may contain the most information about physical processes that drive the
13 GrIS accumulation and mass loss. Therefore, this work focuses on testing the feasibility of
14 using products such as Moderate Resolution Imaging Spectroradiometer (MODIS) IST as an
15 extra source of information to enhance the utility of modelling techniques. The possibility of
16 using additional remotely-sensed data streams (e.g. passive microwave brightness temperature
17 and albedo) will be investigated in future studies.

18 The Greenland Ice Surface Temperature product (GrIS IST) is available from the MODIS
19 Terra satellite (<http://modis-snow-ice.gsfc.nasa.gov/?c=greenland>) and provides up to one
20 (clear-sky) measurement per day at a native resolution of 1.5 km and an accuracy of $\sim 1^\circ$ -
21 1.5°K (Hall et al., 2012). However, cloud contamination and occasional instrument outages
22 play an important role in the availability of the MODIS IST measurements. These two factors
23 along with some other technical and quality considerations can reduce the availability of the
24 IST measurements to less than 10 high quality clear-sky measurements in some months (Hall
25 et al., 2012). In the context of the OSSE used in this work, synthetic IST was generated based
26 on the temporal resolution and acquisition time of the actual GrIS IST product by perturbing
27 the modelled surface temperature with assumed measurement error described below.

28 **3.3 Regional climate model**

29 The a priori (or prior) estimate used in the DA framework in this study is based on output
30 from the regional climate model Modèle Atmosphérique Régional (MAR; Gallée and Schayes

1 (1994) and Gallée and Duynkerke (1997)). The version of the model used here (i.e. MARv2)
 2 has been applied extensively over the GrIS and is described in more detail in previous studies
 3 (Lefebvre et al., 2003; Fettweis et al., 2005). This version has also been used to generate future
 4 projections for the ICE2SEA European project (Fettweis et al., 2013). For this study, MAR
 5 was used to generate hourly near-surface meteorological outputs (i.e., temperature, pressure,
 6 wind speed and direction, longwave and shortwave radiation, precipitation, pressure,
 7 humidity, etc.) at a horizontal spatial resolution of 25 km to force an offline snow/ice model.
 8 The ERA-Interim reanalysis from the European Centre for Medium-Range Weather Forecasts
 9 (ECMWF) was used to initialize the MAR meteorological fields at the beginning of the
 10 simulation (1979) and to force the atmospheric lateral boundaries as well as the oceanic
 11 conditions (surface temperature and sea ice extent) every 6 hours over 1979-2010. MAR was
 12 not reinitialized every day by the ECMWF reanalysis and its results were not recalibrated
 13 after the simulation to better compare with observations as in other approaches (e.g. Box et
 14 al., 2004; Box et al., 2006). The reader is referred to Fettweis et al. (2005), Lefebvre et al.
 15 (2003) and Fettweis et al. (2011) for detailed information on the MAR setup used here.

16 **3.4 Surface mass/energy balance and snow physical model**

17 The key equations related to SMB are the water and energy balance of the near-surface ice
 18 sheet. The bulk surface mass balance for each model pixel (i.e., integrated over the top ~10
 19 meters of the ice sheet) can be written as:

$$20 \quad SMB = P - E + C - R \quad (1)$$

21 where P is the surface precipitation, E is the surface evaporation/sublimation, C includes both
 22 liquid and solid condensation, and R is the meltwater runoff from the snow/icepack. Note that
 23 refreezing is implicitly included in the runoff term. Evaporation, sublimation, condensation
 24 and runoff are the key variables that drive the surface mass loss (SML), while precipitation is
 25 the key meteorological driver for GrIS surface accumulation.

26 The temporal evolution of snow temperature in a vertical snow column is constrained by the
 27 conservation of energy equation, i.e. (Brun et al. 1989):

$$28 \quad \frac{\partial(\rho c_p T)}{\partial t} = \frac{\partial^2(\kappa T)}{\partial z^2} + q \quad (2)$$

1 where ρ is the snow density, c_p is the snow heat capacity, T is the snow temperature at
 2 depth z and time t , and κ is the snow heat conductivity, and q represents a sink (melt) and
 3 source (refreezing). It is worth noting that Eq. (2) is valid for $T < 273.15\text{K}$; any energy inputs
 4 that would raise the temperature beyond freezing instead contribute directly to melt. Equation
 5 (2) is subject to the surface energy balance as a boundary condition, which is the key driver of
 6 the snowpack energy budget:

$$7 \quad R_s^\downarrow(1-\alpha) + R_l^\downarrow - R_l^\uparrow = R_n = Q_{SH} + Q_{LH} + Q_G \quad (3)$$

8 where R_s^\downarrow is the downward shortwave radiation, α is the (broadband) snow albedo, R_l^\downarrow and
 9 R_l^\uparrow are the downward and upward longwave radiation all terms are positive values. R_n is the
 10 net radiation that is partitioned among the surface sensible (Q_{SH}), latent (Q_{LH}), and surface
 11 (Q_G) heat fluxes (into the snow). Q_{SH} and Q_{LH} are positive when directed toward the
 12 atmosphere and Q_G is positive when directed toward the snow/ice surface. Based on Eq.
 13 (3), R_s^\downarrow , R_l^\downarrow , α , and air temperature, specific humidity, and wind speed (embedded in Q_{SH} and
 14 Q_{LH}) are the key meteorological variables controlling the downward energy into the
 15 snowpack (Q_G), which ultimately contributes to runoff (R).

16 The above coupled surface mass/energy balance represented by the CROCUS snow physical
 17 model was used in this study to provide a prior estimate of the GrIS surface mass fluxes that
 18 is consistent with the nominal forcings provided by MAR. CROCUS is a 1D energy balance
 19 model consisting of a thermodynamic module, a water balance module taking into account the
 20 refreezing of meltwater, a turbulent module, a snow metamorphism module, a snow/ice
 21 discretization module and an integrated surface albedo module. CROCUS derives the
 22 turbulent sensible and latent heat fluxes using a bulk method (Brun et al., 1989), which
 23 applies Monin-Obukhov similarity theory to estimate turbulent fluxes using the near-surface
 24 wind speed and the temperature and humidity differences between the surface and the
 25 temperature at ~ 3 m, prescribed by MAR. CROCUS uses the bulk Richardson number to
 26 adapt the fluxes for stable and unstable atmospheric conditions, respectively. Note that a
 27 similar approach has been used by Van den Broeke et al., (2009). CROCUS computes albedo
 28 and absorbed energy in each layer for three spectral bands (i.e. visible, and two near infrared
 29 bands). The capability of the model to partition the incident solar radiation between the layers
 30 allows melt occurs on multiple depths. In CROCUS each snow layer in the snow column is

1 treated as a reservoir with a maximum water holding capacity of 5% of the pore volume.
2 When the liquid water content (LWC) exceeds the threshold, excess water moves toward the
3 layer below and the process continues until the water reaches the bottom layer and generates
4 runoff. In addition, CROCUS takes into account changes in LWC due to snow melt,
5 refreezing, and evaporation during a model time step. The physics of CROCUS and its
6 validation are detailed in Brun et al. (1989, 1992).

7 Assimilation of data into an RCM is another option for attempting to improve RCM fields
8 (such as precipitation, for example), but beyond the scope of this work. The focus of this
9 work is improving of surface mass fluxes using RCM outputs and assimilation of a surface
10 remote sensing data stream. Furthermore, the use of a fully coupled MAR-CROCUS system
11 to generate an a priori ensemble estimate would be computationally prohibitive. To reduce the
12 computational burden, an offline version of CROCUS was implemented (i.e., MAR was run
13 over the whole modelling period, and then MAR outputs were used to force CROCUS over
14 the same period). One can think of the DA framework outlined below as providing an update
15 to an initial (prior) estimate of the surface mass fluxes from MAR (or any other regional
16 climate model) using IST data as an additional constraint.

17 Of particular relevance to this study is the connection between CROCUS states and the
18 measured variables used in the DA (i.e. IST). Surface temperature (synthetic IST) is an output
19 of the forward model (CROCUS), therefore, it can directly be used as a prediction of the
20 measurement in the DA system. One key aspect is that the raw measurements are available at
21 higher spatial resolution than the model state (i.e. 1.5 km vs. 25 km). This was handled via an
22 assumed change in the measurement error due to aggregation as described in more detail
23 below.

24 **3.5 Model adaptation**

25 The CROCUS snow/ice model was originally developed for operational avalanche
26 forecasting. Therefore, the model must be modified for SMB ice sheet applications.
27 Following Fettweis (2006), the bottom boundary condition was modified for simulating
28 approximately the top 10 meters of the ice sheets. In this context, this represents the “surface”
29 mass and energy balance via the vertically integrated states and fluxes within these top layers
30 of the ice sheet. This method consists of the following rules: First, if during the model
31 integration the sum of the snow and ice layer heights becomes less than 8 m, the bottom layer

1 is extended for two meters. Second, in the case that the sum of the snow and ice layer heights
 2 becomes larger than 15 m, the bottom layer is divided by two. This is consistent with the
 3 methodology used in nominal MAR simulations.

4 **3.6 Ensemble Batch Smoother (EnBS) Framework**

5 The EnBS is a technique that conditions a prior estimate of model states on measurements
 6 taken over an assimilation window to generate a posterior reanalysis estimate rather than a
 7 real-time (or sequential) estimate (Giroto et al., 2014a; Bateni et al., 2013, 2015). In the
 8 context of this paper, the assimilation window is a full annual cycle and measurements consist
 9 of IST data over this period. Using the generated forcing fields from MAR, the CROCUS
 10 model was run forward in time to provide an ensemble of a priori estimates of snow/ice state
 11 variables (e.g. surface temperature, snow/ice layer temperature, density, grain size, etc.) and
 12 different surface mass fluxes (e.g. evaporation, sublimation, runoff, etc.). The propagation of
 13 the CROCUS model forward in time can be shown in state-space form as:

$$14 \quad \mathbf{y}_j(t) = f(\mathbf{y}_j(\tau), \mathbf{u}_j(t), \boldsymbol{\beta}_j) \quad (4)$$

15 where $\mathbf{y}_j(t)$ is the vector of states for the j th realization at time t , $f(\cdot)$ represents the
 16 CROCUS model operator, $\mathbf{y}_j(\tau)$ is the vector of states at previous times (τ), $\mathbf{u}_j(t)$ is the
 17 forcing fields for realization j , and $\boldsymbol{\beta}_j$ is the model parameter vector for replicate j .
 18 Conventionally, the generated snow/ice states and surface mass fluxes by the forward
 19 propagation of CROCUS are called the open-loop (prior) estimates. Note that $\mathbf{y}_j(\tau=0)$
 20 represents the initial snow profile (IC: initial condition).

21 The main source of uncertainty in a priori snow/ice states and surface mass fluxes is
 22 hypothesized to be most likely due to errors in the meteorological forcings ($\mathbf{u}_j(t)$, see Eq. 4)
 23 generated by a parent model (in this case MAR): incoming shortwave and longwave radiation,
 24 air temperature (T_a , which is implicit in the latent and sensible heat fluxes), precipitation,
 25 wind speed, relative humidity, and cloudiness. Herein, our focus is on the sub-set of key
 26 forcings that are the postulated main drivers of SMB (i.e., \mathbf{P} , \mathbf{R}_l , \mathbf{R}_s , and T_a). It is
 27 hypothesized that the a priori uncertainty in forcings can be modeled via:

$$28 \quad \mathbf{P}_j(x, t) = \gamma_{P,j}(x) \mathbf{P}_{MAR}(x, t) \quad (5a)$$

$$1 \quad \mathbf{R}_{s,j}^\downarrow(x,t) = \gamma_{s,j}(x) \mathbf{R}_{s,MAR}^\downarrow(x,t) \quad (5b)$$

$$2 \quad \mathbf{R}_{l,j}^\downarrow(x,t) = \gamma_{l,j}(x) \mathbf{R}_{l,MAR}^\downarrow(x,t) \quad (5c)$$

$$3 \quad \mathbf{T}_{a,j}(x,t) = \gamma_{T,j}(x) \mathbf{T}_{a,MAR}(x,t) \quad (5d)$$

4 where $\mathbf{P}_{MAR}(x,t)$, $\mathbf{R}_{s,MAR}^\downarrow(x,t)$, $\mathbf{R}_{l,MAR}^\downarrow(x,t)$, and $\mathbf{T}_{a,MAR}(x,t)$ are the nominal near-surface
5 meteorological outputs from MAR, $\gamma_{p,j}(x)$, $\gamma_{s,j}(x)$, $\gamma_{l,j}(x)$, and $\gamma_{T,j}(x)$ are lognormally-
6 distributed multiplicative coefficients designed to capture uncertainty in the forcing inputs.
7 The subscript j represents an individual ensemble member sampled from the postulated
8 uncertainty distribution ($j = 1, \dots, N_e$, where N_e represents the ensemble size) and x shows
9 the spatial index (i.e., implicitly represents an individual computational pixel in the domain).
10 It should be noted that, a multiplicative lognormal perturbation model (e.g. Margulis et al.,
11 2002; Andreadis and Lettenmaier, 2006; Forman and Margulis, 2010, etc.) was used since all
12 forcing (i.e., \mathbf{P} , \mathbf{R}_l , \mathbf{R}_s , and \mathbf{T}_a [°K]) are positive quantities and it provides a simple
13 mechanism for capturing the expected uncertainty in the inputs. This type of perturbation
14 model characterizes the ensemble using the first two moments (i.e., mean and coefficient of
15 variation (CV)) (Forman and Margulis 2010). In this study, the mean, CV, and cross
16 correlation between the forcing variables was obtained using the reported values in De
17 Lannoy et al. (2010, 2012). All of the parameters for each forcing are shown in Table 1.

18 Traditional DA applications are posed as state estimation problems where the vector of state
19 variables (i.e., snow temperature, density, grain size, depth, etc.) is estimated via conditioning
20 on measurements. In the current application, this can become prohibitive since the state vector
21 dimension is extremely large (i.e., each snow state profile involves 50 layers with several
22 states per pixel and several thousand pixels over the domain). More importantly, updated
23 states do not provide quantitative information about surface mass fluxes. Hence, here we took
24 a different approach. Rather than estimating the states directly, we treated the multiplicative
25 coefficients $\gamma_{i,j}$ in Eq. (5) as the ‘states’ to be estimated. In other words, the multiplicative
26 coefficients have been used to transfer the nominal MAR forcing into probabilistic space (i.e.
27 prior and posterior forcings). The DA algorithm uses IST measurements to condition the
28 probability density function (pdf) of the prior multiplicative coefficients to compute the
29 posterior pdf of the multiplicative coefficients. This strategy, which was also used specifically
30 for precipitation in Durand et al. (2008) and Giroto et al. (2014a), is in direct recognition of

1 the fact that the primary source of uncertainty in surface mass fluxes is due to error in the
 2 near-surface meteorological forcing inputs. The added benefit of this approach is that the size
 3 of the state vector is significantly reduced even in the case of time variant multiplicative
 4 states. Such a strategy derives a posterior estimate of the forcing variables directly (via the
 5 updated $\gamma_{i,j}$), and consequently allows for improved estimates of the surface mass fluxes via
 6 a posterior integration of CROCUS (with the posterior forcing inputs). The DA system
 7 theoretically allows the multiplicative states to vary on any arbitrary time scale. However, for
 8 simplicity, we implemented time-invariant perturbations (i.e., assumed $\gamma_{i,j}$ were unchanged
 9 over the annual modelling period) herein. In this way the update to the states was designed to
 10 allow for biases and/or low-frequency errors in individual realizations in the prior
 11 multiplicative states.

12 It would be ideal to characterize the uncertainties for all inputs from the information content
 13 in the assimilated data stream(s). However, in many cases available measurements are not
 14 relevant to some sources of uncertainty in the models. For instance, in this study, IST is less
 15 likely to have information about precipitation because there is no expected meaningful
 16 correlation between precipitation and IST. With regard to the fact that precipitation cannot be
 17 updated using the IST data the focus of this work has involved constraining the GrIS surface
 18 mass loss (SML) components (i.e., sublimation/evaporation, condensation, and runoff), while
 19 still including the expected uncertainty in the accumulation term (precipitation). In other
 20 words, all forcing inputs were perturbed to take into account their respective postulated
 21 uncertainties, but only longwave, shortwave and surface air temperature coefficients were
 22 updated as part of the assimilation system.

23 In the update step, the EnBS merges IST measurements with prior multiplicative states in
 24 order to generate a posterior estimate of those multiplicative states. In this study, we used an
 25 EnBS, which was implemented in a batch mode over a pre-defined window (i.e., applied over
 26 one year) with a single update. This feature of the EnBS (i.e., the batch mode update) allows
 27 running MAR and CROCUS in an offline mode that could be applied to the historical record.
 28 The open-loop (prior) estimate of the variables of interest (i.e., γ_S , γ_I , and γ_T) were collected
 29 into the state matrix Γ^- . Similarly, the vector of synthetically generated IST measurements
 30 was assembled into a vector:

$$31 \quad \mathbf{T}_{measurement} = \mathbf{T}_{true} + \mathbf{v} \quad (6)$$

1 where \mathbf{v} is the assumed additive white Gaussian error and \mathbf{T}_{true} is the synthetic truth (see
 2 Sect. 4.1). Finally, each ensemble member was updated individually via a Kalman-type
 3 update equation (Durand and Margulis, 2008; Bateni et al., 2013, 2015),

$$4 \quad \mathbf{\Gamma}_j^+ = \mathbf{\Gamma}_j^- + \mathbf{K}[\mathbf{T}_{measurement} + \mathbf{V}_j - \mathbf{T}_{predicted,j}] \quad (7)$$

5 where $\mathbf{\Gamma}_j^-$ and $\mathbf{\Gamma}_j^+$ represent the j th ensemble member before and after the update, respectively,
 6 $\mathbf{T}_{predicted}$ is the matrix of predicted measurements consisting of predicted IST. \mathbf{V} is the
 7 measurement error that was synthetically produced and added to the measurements in order to
 8 avoid correlation among the replicates (Burgers et al. 1998), and \mathbf{K} is the Kalman gain matrix
 9 which is given by

$$10 \quad \mathbf{K} = \mathbf{C}_{IT}[\mathbf{C}_{TT} + \mathbf{C}_V]^{-1} \quad (8)$$

11 where \mathbf{C}_V is the error covariance of the measurements, \mathbf{C}_{IT} is the cross-covariance between
 12 the prior states and predicted measurements, and \mathbf{C}_{TT} is the covariance of the predicted
 13 measurements. In this framework, the state variables are related to the measurements in the
 14 batch through the covariance matrices that are obtained from the ensemble.

15 The update in Eq. (7) can be seen as a projection of measurement-prediction misfits onto the
 16 states. The updated (posterior) multiplicative states were used in Eq. (5) to retrieve updated
 17 (posterior) forcing. The posterior forcings and initial snow profile (I.C.) were used as inputs
 18 in CROCUS to estimate the posterior surface mass fluxes. The proposed methodology can
 19 simply be extended to multiple years by applying the DA sequentially and independently for
 20 each year (e.g. Giroto et al., 2014b) or via applying the DA to a moving window (e.g. Dunne
 21 et al., 2005). A schematic illustration of the methodology is presented in Figure 2. The
 22 proposed methodology can be thought of as a post-processing (reanalysis) of MAR estimates
 23 by constraining the model using independent IST observations.

24

25 **4 Experimental Design**

26 An OSSE or synthetic twin experiment offers a controlled setting in which the true forcing
 27 variables (i.e., γ_s , γ_l , and γ_T) are available. The goal of an OSSE is to evaluate the feasibility
 28 of the new methodology prior to assimilating real space-borne measurements. In an OSSE, a
 29 synthetic true state and corresponding noisy measurements of the system are generated and

1 used to evaluate the feasibility of the DA framework (e.g. Durand and Margulis, 2006; Crow
2 and Ryu, 2009; De Lannoy et al., 2010).

3 **4.1 True selection**

4 The synthetic truth uses realistic input and measurement error characteristics in conjunction
5 with the forward models to generate a realistic realization of the true system. In this study, the
6 synthetic truth was selected as an outlier (defined below) from the generated ensemble due to
7 the fact that errors in forcings can yield differences between a forward model (open-loop)
8 estimate and the true surface mass fluxes.

9 In the OSSE system, traditionally the synthetic true ensemble is chosen from state space
10 trajectory of the forward model (e.g., Crow and Van Loon, 2006; Durand and Margulis, 2006;
11 Bateni et al., 2013). While an alternative approach could involve choosing the synthetic truth
12 from the trajectory space of another well developed RCM model, running multiple RCM
13 models to generate a synthetic truth is prohibitive.

14 The ensemble of forcing data was generated via Eq. (5) for the year 2010 and then the offline
15 CROCUS implementation was run using the ensemble of forcing data to generate estimates of
16 the GrIS surface mass fluxes in 2010. The year 2010 was chosen, at least in part, since it was
17 characterized by an extreme melt rate (Tedesco et al., 2011). Considering the fact that runoff
18 is the main component of the GrIS surface mass loss, the true ensemble (synthetic truth) was
19 selected in a way that the integrated true runoff over the GrIS was an outlier relative to the
20 median of the ensemble simulations. The forcing variables, states, and fluxes corresponding
21 to the synthetic truth were also considered as the true forcings, the true states and the true
22 fluxes respectively. It should be highlighted that in a synthetic DA experiment, any generated
23 realization from the forward model (CROCUS) can be used as the synthetic truth, but one that
24 is significantly different from the prior mean/median allows for a more robust assessment of
25 the value of the assimilated measurements. In other words, in an OSSE the goal is to assess
26 whether a DA framework can replicate the randomly selected true by merging the
27 measurements with the prior (open-loop) estimates.

28 **4.2 Assimilated measurement characteristics**

29 Surface temperature from the forward model can be considered as a close approximation of
30 the remotely-sensed IST. Here, the synthetic DA experiments were designed to mimic reality

1 as much as possible. Hence, the DA system was run with a realistic representation of the
2 temporal frequency of real space-borne IST measurements; e.g. the GrIS IST measurements
3 from MODIS have a daily temporal resolution. However, in many instances daily
4 observations are not available due to cloud contamination, instrument outage, and quality
5 related considerations. To take this issue into account, the number of available daily IST
6 measurements (i.e., synthetic measurements) for assimilation in each month was derived from
7 the spatial average seen in the actual Greenland IST product (e.g., Hall et al., 2012). The days
8 with measurements were selected randomly so that the total number per month was consistent
9 with the real number of available measurements.

10 Since the raw MODIS IST measurements are available at a much finer spatial resolution (i.e.
11 ~ 1.5 km) than the model scale (25 km), the measurements themselves and their error
12 characteristics would require a pre-processing spatial aggregation to match the resolution of
13 computational pixels (~ 25 km). In the context of the OSSE in this study, the synthetic
14 measurements and forward model both have the same spatial resolution therefore there is no
15 need for spatial aggregation of the predicted measurement. However, specification of realistic
16 measurement errors need to take into account the difference in spatial resolution between
17 MODIS IST measurements and the model pixel scale. Measurement errors for MODIS IST at
18 its raw resolution (i.e. 1.5 km) are expected to be $\sim 1^\circ - 1.5^\circ\text{K}$ (e.g. Hall et al., 2012). Hence the
19 measurement errors at the model scale (25 km) are expected to be less than or equal to this
20 value depending on the level of correlation of the measurement errors at the sub-pixel scale.
21 In the case of perfectly uncorrelated sub-pixel measurement errors, the aggregated
22 measurement would be expected to have a measurement error equal to the fine-scale value
23 divided by the number of sub-grid MODIS pixels. Assuming uncorrelated sub-grid errors are
24 likely overly optimistic, we postulated that the measurement error standard deviation of IST at
25 the 25 km scale is 1K.

26 **4.3 Implementation**

27 The feasibility of the new DA system was evaluated via assimilation of IST as follows: A
28 synthetically generated data stream was assimilated within an EnBS framework to assess the
29 information content of the IST and explore whether it can overcome errors in forcing inputs.
30 This was examined by comparing the open-loop and EnBS estimates of multiplicative states
31 with the synthetic truth. Thereafter, the posterior meteorological forcings were fed into
32 CROCUS to estimate the surface mass fluxes. The performance of the EnBS algorithm was

1 further evaluated through the comparison of the posterior estimates with the prior estimates
2 and the true estimate for all surface mass fluxes. It is worth noting that in the OSSE in this
3 study the ensemble size was set to 100 replicates which has been shown to be adequate in
4 previous relevant studies (e.g. Margulis et al., 2002; Huang et al., 2008; Evensen 2009).

5

6 **5 Results**

7 **5.1 Performance of the EnBS via Assimilation of IST**

8 To provide an illustrative example of the methodology, Figure 3a-c shows the distribution of
9 prior (open-loop) and posterior (obtained by assimilating IST) multiplicative state variables
10 corresponding to the different forcings for a sample pixel (the red square in Figure 1) in the
11 ablation zone (latitude 67°N longitude 49.8°W), which is the critical zone in terms of the GrIS
12 surface mass loss. The prior distribution of multiplicative coefficients for each forcing
13 variable is wide, representing the postulated uncertainty in the prior forcings. In contrast,
14 Figure 3a shows that the histogram of the posterior estimates of γ_T is tightly distributed
15 around the true estimate. A narrow distribution around the true estimate means that the DA
16 system uses the information contained in the IST sequence and moves the ensemble members
17 toward the true estimate while reducing the uncertainty of γ_T . The reduction in uncertainty is
18 evident by comparing the base of the posterior histogram with that from the prior estimates.
19 The positive update by the DA system can be explained based on the fact that IST and air
20 temperature are coupled and each one affects the other (Hall et al., 2008). Figure 3b illustrates
21 that the median of the posterior estimate of γ_l agrees well with the corresponding synthetic
22 truth. Incoming longwave radiation is correlated with the effective (near-surface) air
23 temperature and as stated above, IST and surface air temperature are closely tied to each
24 other. Prior to melt, solar radiation goes into heating the snow/ice surface and during the melt
25 period, energy input drives sublimation or evaporation and melt (Box and Steffen 2001).
26 Therefore, it can be stated that IST is positively correlated with the incoming shortwave
27 radiation. The EnBS system takes advantage of this correlation and provides improved
28 estimates of the multiplicative state related to shortwave radiation (Figure 3c).

29 Figure 3d presents the time series of the IST for the prior, posterior, synthetic true, and
30 assimilated measurements during a portion of the assimilation window. For the purpose of

1 illustration, IST data for 10 days during the dry period (January) and beginning of the melt
2 period (April) were selected to show the ability of the algorithm to estimate the true IST
3 (Figure 3d and Figure 3e). It is evident in Figure 3d-e that the EnBS captures the diurnal
4 variability of IST and closely estimates the true IST both during the daytimes and nighttime
5 during the dry and melt periods. Moreover, Figure 3d shows that the EnBS successfully
6 estimates the true IST even when the temporal resolution of the IST measurements
7 significantly decreases. This is important since the IST record shows that there are fewer
8 measurements available during the months of December and January (Hall et al., 2012) where
9 in some years the available measurements during these two months drop to fewer than 10
10 measurements per month. Comparing Figure 3d with Figure 3e also shows that during the
11 month of January when there are fewer IST measurements the posterior estimates are in good
12 agreement with the true IST, however, the uncertainty of the estimates is slightly larger.
13 These results illustrate that information from IST measurements can be exploited to estimate
14 the multiplicative states (i.e. γ_S , γ_I , and γ_T) and consequently the IST.

15 Results for the whole domain are presented in terms of relevant bulk metrics that capture the
16 integrated impact of the forcings. Specifically, the pixel-wise cumulative incoming shortwave
17 and incoming longwave radiation (in MJ/m²/year) were used to represent the total energy
18 input into the ice sheet and provide insight into the surface energy balance of the GrIS. For
19 the air temperature, negative degree-day temperature (NDD) (i.e., cumulative mean daily air
20 temperature for days in which the mean daily air temperature is below 0°C) and the positive
21 degree-day temperature (PDD) (i.e., cumulative mean daily air temperature for days in which
22 the mean daily air temperature is above 0°C) are two other metrics which are indicative of
23 snow accumulation and melt periods, respectively. These bulk metrics were used to evaluate
24 the performance of the DA algorithm over the entire ice sheet using RMSE and an
25 improvement metric.

26 The spatial mean bias and the spatial RMSE of the prior and posterior estimates of the
27 integrated forcing variables over the GrIS were computed using the prior, posterior, and true
28 cumulative longwave, shortwave, and air temperature (i.e., PDD and NDD). Table 2
29 summarizes the spatial mean bias and the spatial RMSE of the different forcing variables. As
30 can be seen for the entire simulation period, the mean bias (RMSE) of cumulative shortwave,
31 longwave, PDD, and NDD are, respectively, 84% (70%), 82% (85%), 94% (71%), and 65%
32 (86%) less than the mean bias (RMSE) of the prior estimates.

1 An alternative method to evaluate the DA system is to determine the contribution of RS data
 2 to the estimate explicitly. Following Durand et al. (2006) and Bateni et al. (2013) an
 3 improvement metric based on the prior and posterior error relative to the true was defined as
 4 follows:

$$5 \quad \kappa_i = \left| \bar{Y}_i(-) - Y_i^{True} \right| - \left| \bar{Y}_i(+) - Y_i^{True} \right| \quad (9)$$

6 where the $\bar{Y}_i(-)$ and $\bar{Y}_i(+)$ represent the cumulative ensemble median of the prior and
 7 posterior estimates of the forcing i respectively and Y_i^{True} is the cumulative synthetic true for
 8 the forcing i . The improvement metric κ_i can be used to interpret the contribution of the IST
 9 measurements to the posterior estimates of the forcing. This formulation suggests a value
 10 greater than 0 when the posterior error is less than the prior error (i.e., measurement improves
 11 the posterior estimates), a value equal to 0 when the prior and posterior errors are equal, and a
 12 value less than 0 when the error in the posterior estimates is greater than that in the prior
 13 estimates (the measurement degrades the posterior estimates). Table 2 shows that IST
 14 measurements make a large contribution to correct the forcing variables. IST contributed an
 15 integrated sum of 452 (MJ/m²/year), 375 (MJ/m²/year), 14 (°C-day), and 257 (°C-day) to
 16 correct the shortwave, longwave, PPD, and NDD. The improvement metric of the PDD is
 17 much smaller than that of the NDD due the fact that there are many fewer days in which the
 18 mean daily near-surface air temperature is above the freezing point.

19 In order to further investigate the performance of the EnBS, the prior errors (i.e., prior - true)
 20 and the posterior errors (i.e., posterior - true) were computed for each forcing variable. Figure
 21 4a-d shows the histograms of the prior and posterior errors for cumulative R_s , R_l , PDD, and
 22 NDD over the spatial domain. The EnBS reduces the uncertainty of the posterior estimates for
 23 all forcing variables and effectively removes any of the prior biases. Therefore, using the
 24 improved surface energy terms to force CROCUS improves vertically integrated melt energy
 25 and enhances the estimates of the states and fluxes over the vertical snow/ice column.

26 **5.2 Updating the SML terms**

27 While updating the forcing variables is the mechanism by which the EnBS transfers
 28 information from IST into the posterior estimates, the main objective of the DA framework in
 29 this study is to assess the feasibility of providing better estimates of the GrIS SML and related
 30 fluxes using the improved forcings. To generate a benchmark for our analysis, CROCUS was

1 run in open-loop mode using the prior forcings (explained above). The SML terms obtained
2 from the prior (open-loop) simulation constitute a basis for evaluation of the methodology
3 implemented in this study. Using the posterior forcing, CROCUS was executed for each grid
4 cell to obtain posterior estimates of surface mass fluxes (i.e., runoff, sublimation /evaporation,
5 and condensation) and consequently SML.

6 Runoff plays an important role in the GrIS net mass loss and is the main component of the
7 GrIS SML. The GrIS meltwater runoff is heavily concentrated in the ablation zone along the
8 ice sheet margin where the width of the ablation zone in the GrIS in some regions is very
9 narrow and does not exceed tens of kilometres. The map of synthetic true runoff (Figure 5a)
10 shows that the west and southwest margins experience the highest rates of runoff that exceeds
11 6 m water equivalent per year. It is worth remembering that the true runoff is an outlier in the
12 context of ensemble modelling as explained previously. Figure 5b-c shows the runoff
13 anomaly for the prior (i.e. prior-true) and the runoff anomaly for the posterior (i.e. posterior-
14 true) respectively. The gray areas represent the percolation and dry snow zones, which do not
15 generally contribute to surface runoff during the simulation period. It should be noted that in
16 this area the snowmelt is not necessarily zero but refreezing can inhibit runoff. The prior
17 anomaly map (Figure 5b) shows that the open-loop simulation consistently underestimates the
18 true runoff across the domain with a strong negative anomaly in the southwest margin (more
19 than 1600 mm water equivalent below the true). Comparing the GrIS margin pixels in the
20 prior and posterior maps (Figure 5b-c) shows that the anomaly of the posterior estimates is
21 significantly lower than that of the prior estimates. Reduced anomalies indicate that the EnBS
22 successfully recovers the true estimates of the runoff in most pixels. However, the posterior
23 results are not perfect and the algorithm slightly underestimates and overestimates runoff in
24 some pixels.

25 Scatter plots of the runoff for the prior and posterior estimates versus the true estimates are
26 illustrated in Figure 5d-e. Each data point in Figure 5d-e represents the ensemble median of
27 the estimate (i.e., prior, posterior) versus the true estimate in a single pixel; and the error bar
28 illustrates the corresponding ensemble interquartile range of the estimates in the same pixel.
29 The scatter plot of the prior runoff shows that almost all data points lie below the 1:1 line,
30 indicating that the prior estimates were significantly biased (by construct in this OSSE). The
31 posterior scatter plot (Figure 5e) displays that the data points are narrowly distributed around
32 the 1:1 line and the error bars are much smaller than that in the prior estimates, implying that

1 the proposed algorithm significantly removes the bias and decreases the uncertainty of the
2 estimates.

3 Sublimation and evaporation play an important role in the GrIS surface mass loss. However, it
4 should be noted that MAR and CROCUS estimate surface sublimation which is considerably
5 smaller than drifting snow sublimation. Lenaerts et al. (2012) reported for the period 1960-
6 2011 on average surface sublimation is responsible for 40% of total sublimation and drifting
7 snow sublimation is responsible for another 60%. Here, the discussion focuses on sublimation
8 rather than evaporation due to the fact that sublimation is one order of magnitude larger than
9 evaporation. The map of synthetic true sublimation (Figure 6a) shows that the west and
10 southwest of the GrIS in the ablation zone experience the largest sublimation rates. Box and
11 Steffen (2001) explained that at the edge of the ice sheet, where slopes become steeper, the
12 katabatic wind accelerates and tends to increase sublimation. Furthermore, the net radiation
13 increases during the summertime, especially at lower latitudes, which in turn generates a
14 vertical temperature gradient and increases the sublimation. Higher energy input also
15 contributes to a positive albedo feedback (e.g. Tedesco et al. 2011) and further increases the
16 sublimation rates. The prior anomaly map (Figure 6b) illustrates that the open-loop model
17 underestimates the sublimation at the ice sheet margin and slightly overestimates it in the ice
18 sheet interior. The results demonstrate that posterior sublimation estimates from the
19 assimilation of IST are much closer to the truth than are the prior estimates (Figure 6c).
20 Comparing the scatter plots of the posterior versus the true estimates with that of the prior
21 versus the true estimates, reveals that the methodology successfully overcomes the bias and
22 significantly reduces the uncertainty of the sublimation estimates and increases the confidence
23 of the results (see Figure 6d-e).

24 Surface solid condensation (deposition) also influences surface mass fluxes of the GrIS by
25 adding mass to the ice sheet. Similar to sublimation, wind and the vertical specific humidity
26 gradient are two key factors that control the deposition. To be more precise, colder
27 temperatures and lower winds enhance the deposition rates. In contrast with sublimation,
28 deposition occurs at night and during winter, mainly due to radiative cooling (Box and Steffen
29 2001). Figure 7a shows that the surface solid condensation (SSC) is greater in the ice sheet
30 interior where winds are weak and there is sufficient moisture in the air column. The high
31 elevation central regions, however, show less condensation due to distance from moisture
32 sources. High speed winds in the ice sheet margins prevent condensation despite the

1 availability of moisture. Figure 7b shows that the prior estimates for SSC is not in good
2 agreement with the truth and that the prior simulation both underestimates and overestimates
3 surface solid condensation across the domain. A comparison between the prior and posterior
4 anomaly maps (Figure 7b-c) suggests that the posterior estimates closely recover the true
5 estimates. Figure 7e shows that the data points are clustered around the 1:1 line; indicating
6 that the EnBS corrects the bias in the prior estimates (Figure 7d). In addition, posterior error
7 bars are significantly smaller than that of the prior error bars, indicating that the EnBS
8 effectively uses the information content of the IST measurements to eliminate the bias and
9 reduce the uncertainties of the posterior estimates.

10 Herein, the SML is defined as the sum of the mass loss terms (i.e. runoff and
11 sublimation/evaporation) and mass gain term (i.e. surface solid condensation) discussed
12 above. Figure 8a shows that SML is greater in the west and southwest of the ice sheet where
13 runoff is the dominant mass loss mechanism and is smaller in the ice sheet interior where
14 mass loss mainly occurs through sublimation. Similar to runoff, the prior anomaly is largely
15 concentrated in the ablation zone and since runoff is roughly two orders of magnitude larger
16 than sublimation and condensation, the anomaly due to these two fluxes is almost
17 undetectable in the anomaly map (see Figure 8b). Comparing the posterior anomaly map
18 (Figure 8c) with that of the prior, clearly shows that the posterior SML is closely matched
19 with the true estimates across the domain. Scatter plots (Figure 8d-e) also confirm that the
20 EnBS effectively removes the bias and increases the confidence level of SML estimates.

21 To provide an integrated picture over the full domain, Figure 9a-d shows the time series of the
22 cumulative runoff, sublimation, surface solid condensation, and SML over the GrIS
23 respectively in 2010. As illustrated in Figure 9a, the true runoff starts in late April and
24 increases rapidly during the melt season (to a cumulative value of 408 mm) until late August.
25 The central tendency of the prior simulation (as indicated by the ensemble median)
26 underestimates the runoff by about 35% owing to errors in the forcing inputs. The posterior
27 estimates show a cumulative runoff of 394 mm over the GrIS, which is in good agreement
28 with the truth. Table 3 shows that the EnBS reduces the spatial mean bias (RMSE) of the prior
29 estimates of runoff by 90% (61%) from -552 mm (646 mm) to -54 mm (250 mm). Note that
30 runoff occurs in the ablation zone therefore the spatial mean bias and spatial RMSE for runoff
31 were computed over the ablation zone. The spatial mean bias and spatial RMSE for
32 sublimation, condensation, and SML were computed over the entire ice sheet. As evident in

1 Figure 9b, sublimation accelerates during the summer season owing to increased energy input
2 to the snow/ice surface. The true estimate suggests that in total net sublimation (i.e.
3 sublimation and evaporation) accounts for about 66 mm (~15%) mass loss over the GrIS. The
4 median of the prior simulation shows a total sublimation loss of ~56 mm which is 10 mm less
5 than the truth. The EnBS significantly improves the results where the posterior median
6 estimate shows a total sublimation of 65 mm. From Table 3 the spatial mean bias (RMSE) of
7 the posterior estimate shows a 90% (64%) reduction relative to the prior. In general surface
8 solid condensation accelerates during the winter and decelerates in the summer season (Figure
9 9c). The true simulation suggests a cumulative SCC of 27 mm, and the median of the prior
10 and posterior estimates are 25 and 27 mm, respectively. The 76% reduction of the spatial
11 RMSE of the posterior estimates and 80% reduction of the spatial mean bias (Table 3) also
12 supports the accuracy of the posterior estimates. Finally, the true SML estimate is 450 mm,
13 the prior and posterior median of SML are 295, 435 mm, respectively. Clearly the posterior
14 SML estimate is in better agreement with the truth. The IST measurements contribute an
15 integrated sum of 140 mm to correct the posterior estimates of the GrIS SML and also reduce
16 the spatial mean bias and the spatial RMSE of the estimates by 90% and 62% respectively
17 (Table 3).

18 A probabilistic approach also provides information about the uncertainty of the estimates.
19 Figure 9a-d show that the prior estimates of all surface mass fluxes have a large ensemble
20 spread, reflecting the propagation of a priori forcing uncertainties to SML terms. During the
21 update process the EnBS significantly reduces the uncertainties of the posterior estimates of
22 forcing variables and consequently the posterior estimates of the surface mass fluxes.
23 Comparing the narrow blue shaded area with the wide red shaded area illustrates that the
24 EnBS increases the confidence of the model predictions by decreasing the error and
25 uncertainties of the posterior estimates relative to the prior estimates.

26 **5.3 Sensitivity to the synthetic truth values**

27 As in any OSSE, the synthetic measurements are, by construct, a function of the chosen true
28 and therefore the posterior results could be impacted by the particular selection of the true
29 realization. To address this concern, and show the robustness of the proposed algorithm, the
30 simulation was repeated for two different true values; one smaller than the baseline simulation
31 and the other larger. In the first case the synthetic true runoff was set to 330 mm, which is the
32 average of the runoff estimates from the open-loop simulation (i.e. ~260 mm) and the true

1 runoff from the baseline simulation (i.e., ~400 mm). In the second case the true runoff was set
2 to 470 mm, which is 70 mm larger than the baseline simulation. Table 4 shows the RMSE of
3 the surface mass fluxes for all simulation cases. The posterior RMSE of each mass flux for all
4 simulation cases are very similar even when the prior RMSE of the estimates are significantly
5 different. For example, the prior RMSE of the runoff (SML) for the second simulation case
6 (true runoff equal to 470 mm) is 2.5 (2.6) times larger than the prior RMSE of the first
7 simulation case (true runoff equal to 330 mm), but the posterior RMSE differs by only 4%
8 (10%). Therefore, it can be stated that the DA algorithm robustly retrieve the true estimates of
9 the surface mass fluxes and the performance of the algorithm is relatively insensitive to the
10 selected truth.

11

12 **6 Discussion and conclusions**

13 A new data assimilation methodology for improving estimates of the GrIS surface mass loss
14 fluxes has been tested and presented using an observing system simulation experiment
15 framework. The prior estimates were derived from an offline surface module (CROCUS)
16 forced by an ensemble of meteorological forcing fields that were based on a nominal regional
17 climate model simulation (in this case MAR). A posterior estimate was generated by
18 conditioning the forcings on the synthetically generated IST measurements using an ensemble
19 batch smoother (EnBS) approach. Specifically, it was shown that using the EnBS with IST
20 measurements was able to improve nominal estimates derived from MAR that result from
21 erroneous forcing fields that drive surface mass and energy balance processes. The results
22 illustrated that IST measurements have potential information on shortwave, longwave, and
23 surface air temperature that allows for correction of errors in these terms. However, due to the
24 lack of meaningful correlation between precipitation and IST measurements, the precipitation
25 flux was not updated in this context (i.e. the prior and posterior precipitation is the same).
26 Hence the assimilation of IST is primarily beneficial for estimating the surface mass loss
27 terms and not the accumulation term. However, it should be noted that, using MAR-CROCUS
28 to generate the synthetic truth might lead to optimistic results since the truth is taken from the
29 same model. Mitigation of this was attempted by using an outlier for the truth. An expensive
30 alternative, but worth pursuing in future work, would be to use other RCM models to generate
31 the synthetic truth. That said, it can be argued that using another model such as RACMO2
32 (Ettema et al., 2009) to generate the true realization will not significantly affect the results

1 because the synthetic truth from RACMO2 is likely to fall within the ensemble spread of
2 MAR-CROCUS trajectory. The main reasons for that are (1) the SMB fluxes from MAR and
3 RACMO2 are highly correlated (Fettweis et al., 2013), (2) the trends of SMB fluxes from two
4 models are very similar Vernon et al., (2013). Furthermore, sensitivity analysis shows that
5 the proposed algorithm is able to retrieve the synthetic truth for the extreme cases where the
6 real true stats fall beyond the chosen values.

7 The new methodology has several advantages over the traditional state-space data
8 assimilation approaches. First, in this new application the multiplicative perturbation variables
9 are considered as states to be updated. Reduction of the size of the state vector and
10 consequently computational costs is the direct outcome of this approach. Second, mass loss
11 terms cannot directly be sensed by the means of satellite sensors; using this methodology, the
12 mass loss fluxes were estimated indirectly by reducing the error in forcing variables. Finally,
13 the modularity of the proposed methodology would allow for incorporation of any regional
14 climate model and additional remotely-sensed observations in future applications. All of these
15 advantages should make such data assimilation approaches an attractive and complementary
16 approach to better resolve and diagnose the ice sheet surface mass fluxes. The improved mass
17 loss estimates could also be used as input to net mass balance estimates and ultimately a sea
18 level rise projection when applied to real data over the remote sensing record.

19 As a final note, it should be emphasized that the application presented in this study does not
20 attempt to optimize or include uncertainty in any model parameters. Rather, the focus is on
21 the uncertainty of time-varying model forcing inputs, which is expected to be the primary
22 source of uncertainty in estimates of surface melt. We acknowledge that the model parameters
23 are treated as certain and therefore, any uncertainty/error in model parameters (e.g., water
24 holding capacity that impacts the transformation of meltwater into runoff) would increase the
25 expected error in posterior SML in an application with real data. A more general case where
26 estimation of parameters is included in the data assimilation framework could be the basis of
27 future work.

28 The next logical step is to apply the methodology with real IST measurements to further
29 validate the robustness of the proposed approach. This future work will include the use of the
30 MODIS IST product for estimating GrIS SML. The data assimilation framework is general
31 and could also include the potential application of assimilation of passive microwave, albedo,

1 and even Gravity Recovery and Climate Experiment (GRACE) data to further constrain GrIS
2 SMB estimates.

3

4 **Acknowledgements**

5 This work was partially sponsored by NSF through grant #0909388. We thank Samuel Morin
6 (Météo-France) and Dorothy Hall (NASA Goddard Space Flight Center) for input on the
7 CROCUS model and IST product respectively. The authors would also like to thank two
8 anonymous reviewers for their helpful comments on the manuscript.

9

1 References

- 2 Abdalati, W. and Steffen, K.: Passive microwave derived snow melt regions on the Greenland
3 Ice Sheet, *Geophys. Res. Lett.*, 22(7), 787–790, 1995.
- 4 Abdalati, W. and Steffen, K.: Snowmelt on the Greenland Ice Sheet as Derived from Passive
5 Microwave Satellite Data, *J. Clim.*, 10(2), 165–175, 1997.
- 6 Abdalati, W. and Steffen, K.: Greenland ice sheet melt extent: 1979-1999, 106(D24), 983–
7 988, 2001.
- 8 Al-Yaari, a., Wigneron, J.-P., Ducharne, a., Kerr, Y., de Rosnay, P., de Jeu, R., Govind, a., Al
9 Bitar, a., Albergel, C., Muñoz-Sabater, J., Richaume, P. and Mialon, a.: Global-scale
10 evaluation of two satellite-based passive microwave soil moisture datasets (SMOS and
11 AMSR-E) with respect to Land Data Assimilation System estimates, *Remote Sens. Environ.*,
12 149, 181–195, doi:10.1016/j.rse.2014.04.006, 2014.
- 13 Andreadis, K. M. and Lettenmaier, D. P.: Assimilating remotely sensed snow observations
14 into a macroscale hydrology model, *Adv. Water Resour.*, 29(6), 872–886,
15 doi:10.1016/j.advwatres.2005.08.004, 2006.
- 16 Bamber, J. L. and Layberry, R. L.: 1 . Measurement , data reduction , and errors ice sheet was
17 reestimated and found to have a value at a sample, *J. Geophys. Res.*, 106(D24), 33773–33780,
18 2001.
- 19 Bateni, S., Huang, C. and Margulis, S.: Feasibility of Characterizing Snowpack and the
20 Freeze–Thaw State of Underlying Soil Using Multifrequency Active/Passive Microwave
21 Data, , 51(7), 4085–4102, 2013.
- 22 Bateni, S., Margulis, S., Podest, E. and McDonald, K.: Characterizing Snowpack and the
23 Freeze–Thaw State of Underlying Soil via Assimilation of Multifrequency Passive/Active
24 Microwave Data: A Case Study (NASA CLPX 2003) , 53(1), 173–189 , 2015.
- 25 Box, J. E.: Greenland ice sheet surface mass balance 1991–2000: Application of Polar MM5
26 mesoscale model and in situ data, *J. Geophys. Res.*, 109(D16), D16105,
27 doi:10.1029/2003JD004451, 2004.
- 28 Box, J. E., Bromwich, D. H., Veenhuis, B. a., Bai, L.-S., Stroeve, J. C., Rogers, J. C., Steffen,
29 K., Haran, T. and Wang, S.-H.: Greenland Ice Sheet Surface Mass Balance Variability (1988–

1 2004) from Calibrated Polar MM5 Output, *J. Clim.*, 19(12), 2783–2800,
2 doi:10.1175/JCLI3738.1, 2006.

3 Box, J. E., Fettweis, X., Stroeve, J. C., Tedesco, M., Hall, D. K. and Steffen, K.: Greenland
4 ice sheet albedo feedback: thermodynamics and atmospheric drivers, *Cryosph.*, 6(4), 821–
5 839, doi:10.5194/tc-6-821-2012, 2012.

6 Box, J. E. and Steffen, K.: Sublimation on the Greenland ice sheet from automated weather
7 station observations, *J. Geophys. Res.*, 106(D24), 33965–33981, doi:10.1029/2001JD900219,
8 2001.

9 Brun, B. E., Martin, E., Simon, V. and Gendre, C.: An energy and mass model of snow cover
10 sidtable for operational avalanche forecasting, 35(12), 333–342, 1989.

11 Brun, E., David, P., Sudul, M. and Brunot, G.: A numerical model to simulate snow-cover
12 stratigraphy for operational avalanche forecasting, *J. Glaciol.*, 38(128), 13–22, 1992.

13 Burgers, G., Jan van Leeuwen, P. and Evensen, G.: Analysis Scheme in the Ensemble Kalman
14 Filter, *Mon. Weather Rev.*, 126(6), 1719–1724, doi:10.1175/1520-
15 0493(1998)126<1719:ASITEK>2.0.CO;2, 1998.

16 Crow, W. T. and Ryu, D.: A new data assimilation approach for improving runoff prediction
17 using remotely-sensed soil moisture retrievals, *Hydrol. Earth Syst. Sci.*, 13(1), 1–16,
18 doi:10.5194/hess-13-1-2009, 2009.

19 Crow, W. T. and Van Loon, E.: Impact of Incorrect Model Error Assumptions on the
20 Sequential Assimilation of Remotely Sensed Surface Soil Moisture, *J. Hydrometeorol.*, 7(3),
21 421–432, doi:10.1175/JHM499.1, 2006.

22 Cuffey, K. M., and Paterson, W. S. B.: *The physics of glaciers*, 4th edition, Academic Press,
23 United States of America, 704pp, 2010.

24 De Lannoy, G. J. M., Reichle, R. H., Arsenault, K. R., Houser, P. R., Kumar, S., Verhoest, N.
25 E. C. and Pauwels, V. R. N.: Multiscale assimilation of Advanced Microwave Scanning
26 Radiometer–EOS snow water equivalent and Moderate Resolution Imaging
27 Spectroradiometer snow cover fraction observations in northern Colorado, *Water Resour.*
28 *Res.*, 48(1), W01522, doi:10.1029/2011WR010588, 2012.

29 De Lannoy, G. J. M., Reichle, R. H., Houser, P. R., Arsenault, K. R., Verhoest, N. E. C. and
30 Pauwels, V. R. N.: Satellite-Scale Snow Water Equivalent Assimilation into a High-

1 Resolution Land Surface Model, *J. Hydrometeorol.*, 11(2), 352–369,
2 doi:10.1175/2009JHM1192.1, 2010.

3 Dunne, S. and Entekhabi, D.: An ensemble-based reanalysis approach to land data
4 assimilation, *Water Resour. Res.*, 41(2), 1–18, doi:10.1029/2004WR003449, 2005.

5 Durand, M., Kim, E. J. and Margulis, S. a.: Radiance assimilation shows promise for
6 snowpack characterization, *Geophys. Res. Lett.*, 36(2), 1–5, doi:10.1029/2008GL035214,
7 2009.

8 Durand, M. and Margulis, S.: Feasibility test of multifrequency radiometric data assimilation
9 to estimate snow water equivalent, *J. Hydrometeorol.*, 443–457,
10 doi: <http://dx.doi.org/10.1175/JHM502.1>, 2006.

11 Durand, M. and Margulis, S. a.: Effects of uncertainty magnitude and accuracy on
12 assimilation of multiscale measurements for snowpack characterization, *J. Geophys. Res.*,
13 113(D2), 1–17, doi:10.1029/2007JD008662, 2008.

14 Durand, M., Molotch, N. P. and Margulis, S. a.: A Bayesian approach to snow water
15 equivalent reconstruction, *J. Geophys. Res.*, 113(D20), 1–15, doi:10.1029/2008JD009894,
16 2008.

17 Enderlin, E. M., Howat, I. M., Jeong, S., Noh, M.-J., van Angelen J. H., and van den Broeke,
18 M. R.: An improved mass budget for the Greenland ice sheet. *Geophys. Res. Lett.*, 41, 866–
19 872, doi:10.1002/2013GL059010, 2014.

20 Ettema, J., van den Broeke, M. R., van Meijgaard, E., van de Berg, W. J., Bamber, J. L., Box,
21 J. E. and Bales, R. C.: Higher surface mass balance of the Greenland ice sheet revealed by
22 high-resolution climate modeling, *Geophys. Res. Lett.*, 36(12), 1–5,
23 doi:10.1029/2009GL038110, 2009.

24 Ettema, J., van den Broeke, M. R., van Meijgaard, E., van de Berg, W. J., Box, J. E. and
25 Steffen, K.: Climate of the Greenland ice sheet using a high-resolution climate model – Part
26 1: Evaluation, *Cryosph.*, 4(4), 511–527, doi:10.5194/tc-4-511-2010, 2010.

27 Evensen, G. : *Data Assimilation: The Ensemble Kalman Filter*, 2nd edition, Springer,
28 307pp, 2009.

29 Fettweis, X., Franco, B., Tedesco, M., van Angelen, J. H., Lenaerts, J. T. M., van den Broeke,
30 M. R. and Gallée, H.: Estimating the Greenland ice sheet surface mass balance contribution to

1 future sea level rise using the regional atmospheric climate model MAR, *Cryosph.*, 7(2), 469–
2 489, doi:10.5194/tc-7-469-2013, 2013.

3 Fettweis, X., Gallée, H., Lefebvre, F. and Ypersele, J.-P.: Greenland surface mass balance
4 simulated by a regional climate model and comparison with satellite-derived data in 1990–
5 1991, *Clim. Dyn.*, 24(6), 623–640, doi:10.1007/s00382-005-0010-y, 2005.

6 Fettweis X. :Reconstruction of the 1979-2005 greenland ice sheet surface mass balance using
7 satellite data and the regional climate model MAR, PhD thesis, Université catholique de
8 Louvain, Leuven, Belgium, 2006.

9 Fettweis, X., Tedesco, M., van den Broeke, M. and Ettema, J.: Melting trends over the
10 Greenland ice sheet (1958–2009) from spaceborne microwave data and regional climate
11 models, *Cryosph.*, 5(2), 359–375, doi:10.5194/tc-5-359-2011, 2011.

12 Fettweis, X., van Ypersele, J.-P., Gallée, H., Lefebvre, F. and Lefebvre, W.: The 1979–2005
13 Greenland ice sheet melt extent from passive microwave data using an improved version of
14 the melt retrieval XPGR algorithm, *Geophys. Res. Lett.*, 34(5), 1–5,
15 doi:10.1029/2006GL028787, 2007.

16 Forman, B. a. and Margulis, S. a.: Assimilation of multiresolution radiation products into a
17 downwelling surface radiation model: 1. Prior ensemble implementation, *J. Geophys. Res.*,
18 115(D22), 1–14, doi:10.1029/2010JD013920, 2010.

19 Franco, B., Fettweis, X. and Erpicum, M.: Future projections of the Greenland ice sheet
20 energy balance driving the surface melt, *Cryosph.*, 7(1), 1–18, doi:10.5194/tc-7-1-2013, 2013.

21 Franz, K. J., Hogue, T. S., Barik, M. and He, M.: Assessment of SWE data assimilation for
22 ensemble streamflow predictions, *J. Hydrol.*, 519, 2737–2746,
23 doi:10.1016/j.jhydrol.2014.07.008, 2014.

24 Gallée, H. and Duynkerke, P.: Air-snow interactions and the surface energy and mass balance
25 over the melting zone of west Greenland during the Greenland Ice Margin Experiment, *J.*
26 *Geophys. Res.*, 102(D12), 13813–13824, 1997.

27 Gallée, H. and Schayes, G.: Development of a Three-Dimensional Meso- γ Primitive Equation
28 Model: Katabatic Winds Simulation in the Area of Terra Nova Bay, Antarctica, *Mon.*
29 *Weather Rev.*, 122(4), 671–685, doi:10.1175/1520-0493(1994)122<0671:DOATDM>2.0.
30 CO;2, 1994.

- 1 Giroto, M., Cortés, G., Margulis, S. A. and Durand, M.: Examining spatial and temporal
2 variability in snow water equivalent using a 27 year reanalysis: Kern River watershed, Sierra
3 Nevada, *Water Resour. Res.*, 50(4), 446, doi:10.1002/2014WR015346, 2014.
- 4 Giroto, M., Margulis, S. and Durand, M.: Probabilistic SWE reanalysis as a generalization of
5 deterministic SWE reconstruction techniques, *Hydrol. Process.*, 28(12), 3875–3895,
6 doi:10.1002/hyp.9887, 2014.
- 7 Goldberg, D. N. and Heimbach, P.: Parameter and state estimation with a time-dependent
8 adjoint marine ice sheet model, *Cryosph.*, 7(6), 1659–1678, doi:10.5194/tc-7-1659-2013,
9 2013.
- 10 Hall, D., Box, J., Casey, K., Hook, S., Shuman, C. and Steffen, K.: Comparison of satellite-
11 derived and in-situ observations of ice and snow surface temperatures over Greenland,
12 *Remote Sens. Environ.*, 112(10), 3739–3749, doi:10.1016/j.rse.2008.05.007, 2008.
- 13 Hall, D. K., Comiso, J. C., DiGirolamo, N. E., Shuman, C. a., Box, J. E. and Koenig, L. S.:
14 Variability in the surface temperature and melt extent of the Greenland ice sheet from
15 MODIS, *Geophys. Res. Lett.*, 40(10), 2114–2120, doi:10.1002/grl.50240, 2013.
- 16 Hall, D. K., Comiso, J. C., Digirolamo, N. E., Shuman, C. a., Key, J. R. and Koenig, L. S.: A
17 satellite-derived climate-quality data record of the clear-sky surface temperature of the
18 greenland ice sheet, *J. Clim.*, 25(14), 4785–4798, doi:10.1175/JCLI-D-11-00365.1, 2012.
- 19 Hall, D. K., Nghiem, S. V., Schaaf, C. B., DiGirolamo, N. E. and Neumann, G.: Evaluation of
20 surface and near-surface melt characteristics on the Greenland ice sheet using MODIS and
21 QuikSCAT data, *J. Geophys. Res.*, 114(F4), 1–13, doi:10.1029/2009JF001287, 2009.
- 22 Hall, D. K., Williams, R. S., Casey, K. a., DiGirolamo, N. E. and Wan, Z.: Satellite-derived,
23 melt-season surface temperature of the Greenland Ice Sheet (2000–2005) and its relationship
24 to mass balance, *Geophys. Res. Lett.*, 33(11), L11501, doi:10.1029/2006GL026444, 2006.
- 25 Hanna, E. and Huybrechts, P.: Runoff and mass balance of the Greenland ice sheet: 1958–
26 2003, *J. Geophys. Res.*, 110(D13), 1–16, doi:10.1029/2004JD005641, 2005.
- 27 Hanna, E., Huybrechts, P., Cappelen, J., Steffen, K., Bales, R. C., Burgess, E., McConnell, J.
28 R., Peder Steffensen, J., Van den Broeke, M., Wake, L., Bigg, G., Griffiths, M. and Savas, D.:
29 Greenland Ice Sheet surface mass balance 1870 to 2010 based on Twentieth Century

1 Reanalysis, and links with global climate forcing, *J. Geophys. Res.*, 116(D24),121,
2 doi:10.1029/2011JD016387, 2011.

3 Hanna, E., Jones, J. M., Cappelen, J., Mernild, S. H., Wood, L., Steffen, K. and Huybrechts,
4 P.: The influence of North Atlantic atmospheric and oceanic forcing effects on 1900-2010
5 Greenland summer climate and ice melt/runoff, *Int. J. Climatol.*, 33(4), 862–880,
6 doi:10.1002/joc.3475, 2013.

7 Hook, S. and Vaughan, R.: in-flight validation of mid infrared and thermal infrared data from
8 ASTER and MODIS on the Terra spacecraft using the Lake Tahoe, CA/NV, USA, automated
9 validation, *IEEE Trans. Geosci. Remote Sens.*, 45(6), 1798–1807,
10 doi:10.1109/TGRS.2007.894564, 2007.

11 Huang, C., Li, X. and Lu, L.: Retrieving soil temperature profile by assimilating MODIS LST
12 products with ensemble Kalman filter, *Remote Sens. Environ.*, 112(4), 1320–1336,
13 doi:10.1016/j.rse.2007.03.028, 2008.

14 Khan, S. a., Kjær, K. H., Bevis, M., Bamber, J. L., Wahr, J., Kjeldsen, K. K., Bjørk, A. a.,
15 Korsgaard, N. J., Stearns, L. a., van den Broeke, M. R., Liu, L., Larsen, N. K. and Muresan, I.
16 S.: Sustained mass loss of the northeast Greenland ice sheet triggered by regional warming,
17 *Nat. Clim. Chang.*, 4(4), 292–299, doi:10.1038/nclimate2161, 2014.

18

19 Larour, E., Utke, J., Csatho, B., Schenk, a., Seroussi, H., Morlighem, M., Rignot, E., Schlegel,
20 N. and Khazendar, a.: Inferred basal friction and surface mass balance of the Northeast
21 Greenland Ice Stream using data assimilation of ICESat (Ice Cloud and land Elevation
22 Satellite) surface altimetry and ISSM (Ice Sheet System Model), *Cryosph.*, 8(6), 2335–2351,
23 doi:10.5194/tc-8-2335-2014, 2014.

24 Lefebre, F.: Modeling of snow and ice melt at ETH Camp (West Greenland): A study of
25 surface albedo, *J. Geophys. Res.*, 108(D8), 4231, doi:10.1029/2001JD001160, 2003.

26 Lenaerts, J. T. M., van den Broeke, M. R., van Angelen, J. H., van Meijgaard, E. and Déry, S.
27 J.: Drifting snow climate of the Greenland ice sheet: a study with a regional climate model,
28 *Cryosph.*, 6(4), 891–899, doi:10.5194/tc-6-891-2012, 2012.

29 Lewis, S. and Smith, L.: Hydrologic drainage of the Greenland ice sheet, *Hydrol. Process.*,
30 2011(May 2009), 2004–2011, doi:10.1002/hyp, 2009.

1 Margulis, S. a., McLaughlin, D., Entekhabi, D. and Dunne, S.: Land data assimilation and
2 estimation of soil moisture using measurements from the Southern Great Plains 1997 Field
3 Experiment, *Water Resour. Res.*, 38(12), 35–1–35–18, doi:10.1029/2001WR001114, 2002.

4 Morlighem, M., Seroussi, H., Larour, E. and Rignot, E.: Inversion of basal friction in
5 Antarctica using exact and incomplete adjoints of a higher-order model, *J. Geophys. Res.*
6 *Earth Surf.*, 118(3), 1746–1753, doi:10.1002/jgrf.20125, 2013.

7 Rae, J. G. L., Aðalgeirsdóttir, G., Edwards, T. L., Fettweis, X., Gregory, J. M., Hewitt, H. T.,
8 Lowe, J. a., Lucas-Picher, P., Mottram, R. H., Payne, a. J., Ridley, J. K., Shannon, S. R., van
9 de Berg, W. J., van de Wal, R. S. W. and van den Broeke, M. R.: Greenland ice sheet surface
10 mass balance: evaluating simulations and making projections with regional climate models,
11 *Cryosph.*, 6(6), 1275–1294, doi:10.5194/tc-6-1275-2012, 2012.

12 Rahmstorf, S., Box, J. E., Feulner, G., Mann, M. E., Robinson, A., Rutherford, S. and
13 Schaffernicht, E. J.: Exceptional twentieth-century slowdown in Atlantic Ocean overturning
14 circulation, *Nat. Clim. Chang.*, 5(May), doi:10.1038/nclimate2554, 2015.

15 Reichle, R. H., McLaughlin, D. B. and Entekhabi, D.: Hydrologic Data Assimilation with the
16 Ensemble Kalman Filter, *Mon. Weather Rev.*, 130(1), 103–114, doi:10.1175/1520-
17 0493(2002)130<0103:HDAWTE>2.0.CO;2, 2002.

18 Rignot, E., Box, J. E., Burgess, E. and Hanna, E.: Mass balance of the Greenland ice sheet
19 from 1958 to 2007, *Geophys. Res. Lett.*, 35(20), L20502, doi:10.1029/2008GL035417, 2008.

20 Rignot, E., Velicogna, I., van den Broeke, M. R., Monaghan, a. and Lenaerts, J. T. M.:
21 Acceleration of the contribution of the Greenland and Antarctic ice sheets to sea level rise,
22 *Geophys. Res. Lett.*, 38, L05503, doi:10.1029/2011GL046583, 2011.

23 Smith, L. C., Chu, V. W., Yang, K., Gleason, C. J., Pitcher, L. H., Rennermalm, A. K.,
24 Legleiter, C. J., Behar, A. E., Overstreet, B. T., Moustafa, S. E., Tedesco, M., Forster, R. R.,
25 LeWinter, A. L., Finnegan, D. C., Sheng, Y. and Balog, J.: Efficient meltwater drainage
26 through supraglacial streams and rivers on the southwest Greenland ice sheet, *Proc. Natl.*
27 *Acad. Sci.*, 2000, 201413024, doi:10.1073/pnas.1413024112, 2015.

28 Straneo, F. and Heimbach, P.: North Atlantic warming and the retreat of Greenland’s outlet
29 glaciers., *Nature*, 504(7478), 36–43, doi:10.1038/nature12854, 2013.

1 Tedesco, M.: Snowmelt detection over the Greenland ice sheet from SSM/I brightness
2 temperature daily variations, *Geophys. Res. Lett.*, 34(2), 1–6, doi:10.1029/2006GL028466,
3 2007.

4 Tedesco, M., Fettweis, X., van den Broeke, M. R., van de Wal, R. S. W., Smeets, C. J. P. P.,
5 van de Berg, W. J., Serreze, M. C. and Box, J. E.: The role of albedo and accumulation in the
6 2010 melting record in Greenland, *Environ. Res. Lett.*, 6(1), 014005, doi:10.1088/1748-
7 9326/6/1/014005, 2011.

8 Tedesco, M., Fettweis, X., Mote, T., Wahr, J., Alexander, P., Box, J. E. and Wouters, B.:
9 Evidence and analysis of 2012 Greenland records from spaceborne observations, a regional
10 climate model and reanalysis data, *Cryosph.*, 7(2), 615–630, doi:10.5194/tc-7-615-2013,
11 2013.

12 Tedesco, M., Serreze, M. and Fettweis, X.: Diagnosing the extreme surface melt event over
13 southwestern Greenland in 2007, *Cryosph. Discuss.*, 2(3), 383–397, doi:10.5194/tcd-2-383-
14 2008, 2008.

15 Vernon, C. L., Bamber, J. L., Box, J. E., van den Broeke, M. R., Fettweis, X., Hanna, E. and
16 Huybrechts, P.: Surface mass balance model intercomparison for the Greenland ice sheet,
17 *Cryosph.*, 7(2), 599–614, doi:10.5194/tc-7-599-2013, 2013.

18 Van Angelen, J. H., Lenaerts, J. T. M., Lhermitte, S., Fettweis, X., Kuipers Munneke, P., van
19 den Broeke, M. R., van Meijgaard, E. and Smeets, C. J. P. P.: Sensitivity of Greenland Ice
20 Sheet surface mass balance to surface albedo parameterization: a study with a regional climate
21 model, *Cryosph.*, 6(5), 1175–1186, doi:10.5194/tc-6-1175-2012, 2012.

22 Van de Wal, R. S. W., Boot, W., Smeets, C. J. P. P., Snellen, H., van den Broeke, M. R. and
23 Oerlemans, J.: Twenty-one years of mass balance observations along the K-transect, West
24 Greenland, *Earth Syst. Sci. Data*, 4(1), 31–35, doi:10.5194/essd-4-31-2012, 2012.

25 Van den Broeke, M., Bamber, J., Ettema, J., Rignot, E., Schrama, E., van de Berg, W. J., van
26 Meijgaard, E., Velicogna, I. and Wouters, B.: Partitioning recent Greenland mass loss.,
27 *Science*, 326(5955), 984–6, doi:10.1126/science.1178176, 2009.

28 Van den Broeke, M., Smeets, P. and Ettema, J.: Surface layer climate and turbulent exchange
29 in the ablation zone of the west Greenland ice sheet, *Int. J. Climatol.*, 29(15), 2309–2323,
30 doi:10.1002/joc.1815, 2009.

- 1 Wouters, B., Bamber, J. L., van den Broeke, M. R., Lenaerts, J. T. M. and Sasgen, I.: Limits
2 in detecting acceleration of ice sheet mass loss due to climate variability, *Nat. Geosci.*, 6(8),
3 613–616, doi:10.1038/ngeo1874, 2013.
- 4 Xu, T., Liu, S., Liang, S. and Qin, J.: Improving Predictions of Water and Heat Fluxes by
5 Assimilating MODIS Land Surface Temperature Products into the Common Land Model, *J.*
6 *Hydrometeorol.*, 12(2), 227–244, doi:10.1175/2010JHM1300.1, 2011.
- 7 Zhang, Y.-F., Hoar, T. J., Yang, Z.-L., Anderson, J. L., Toure, A. M. and Rodell, M.:
8 Assimilation of MODIS snow cover through the Data Assimilation Research Testbed and the
9 Community Land Model version 4, *J. Geophys. Res. Atmos.*, 119, 7091–7103,
10 doi:10.1002/2013JD021329, 2014.
- 11

1 Table 1: Postulated parameters (Coefficient of variation (CV) and cross-correlation) for
 2 multiplicative perturbations to hourly meteorological forcing inputs (the units for each forcing
 3 are: P in mm/hour, R_s and R_l in W/m^2 and T_a in K).

Perturbation	CV	Cross correlation			
		P	R_s	R_l	T_a
Precipitation (P)	0.5	1.0	-0.1	0.5	-0.1
Shortwave (R_s)	0.2	-0.1	1.0	-0.3	0.3
Longwave (R_l)	0.1	0.5	-0.3	1.0	0.6
Air temperature (T_a)	0.005	-0.1	0.3	0.6	1.0

4

5

6

7

1 Table 2 : The spatial mean bias, the spatial RMSE, and improvement metric κ for the prior
 2 and posterior estimates of the forcing variables via assimilation of IST over the entire GrIS.

	R_s [MJ/m ² /yr]	R_l [MJ/m ² /yr]	PDD [°C-day]	NDD [°C-day]
Prior Bias	-82.0	-25.6	-16.7	-8.0
Posterior Bias	-12.8	+4.6	-1.0	-2.8
Prior RMSE	791.6	549.1	33.3	394.6
Posterior RMSE	241.3	97.9	9.7	55.4
κ	452.2	375.0	13.8	257.0

3
 4
 5
 6
 7
 8

1 Table 3: The spatial mean bias and the spatial RMSE of runoff, sublimation/evaporation,
 2 surface solid condensation, and net mass loss estimates via assimilation of IST measurements.
 3 The spatial mean bias and the spatial RMSE for runoff were computed over the ablation zone
 4 and for the other surface mass fluxes were computed over the entire ice sheet.

	Runoff	Sublimation	SSC	Surface mass loss
	[mmWE]	[mmWE]	[mmWE]	[mmWE]
Prior Bias	-551.6	-3.1	-0.5	-38.9
Posterior Bias	-54.0	-0.3	-0.1	-3.8
Prior RMSE	646.1	14.7	4.6	174.1
Posterior RMSE	249.8	5.3	1.1	66.9

5
 6
 7
 8

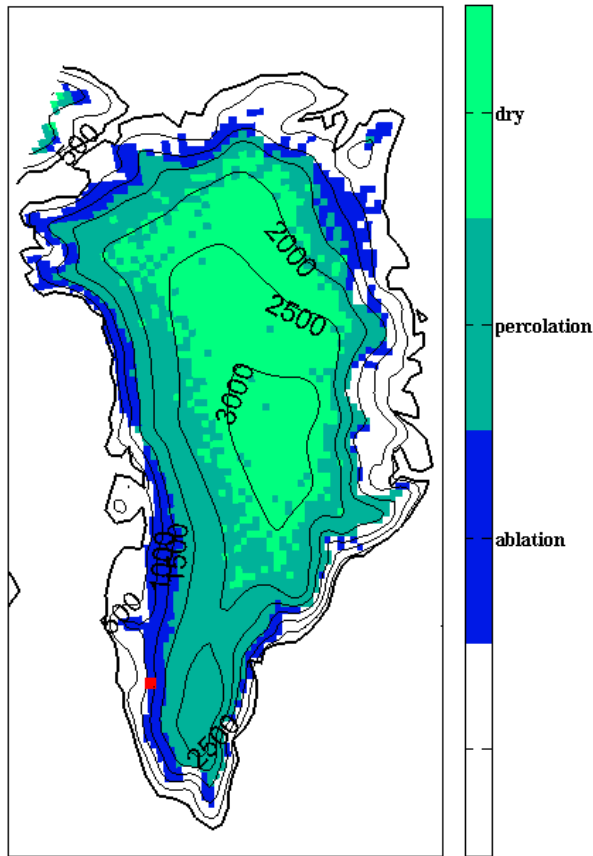
1 Table 4: The spatial RMSE of runoff, sublimation/evaporation, surface solid condensation,
 2 and net mass loss estimates via assimilation of IST measurements for three different true
 3 values.

True Runoff [mm]		Runoff [mm]	Sublimation [mm]	SSC [mm]	Surface mass loss [mm]
330	Prior	348.9	13.4	4.7	92.8
	Posterior	249.2	4.8	1.1	63.6
400 (baseline)	Prior	646.1	14.7	4.6	174.1
	Posterior	249.8	5.3	1.1	66.9
470	Prior	894.4	16.0	4.6	245.1
	Posterior	259.4	5.2	1.1	70.7

4

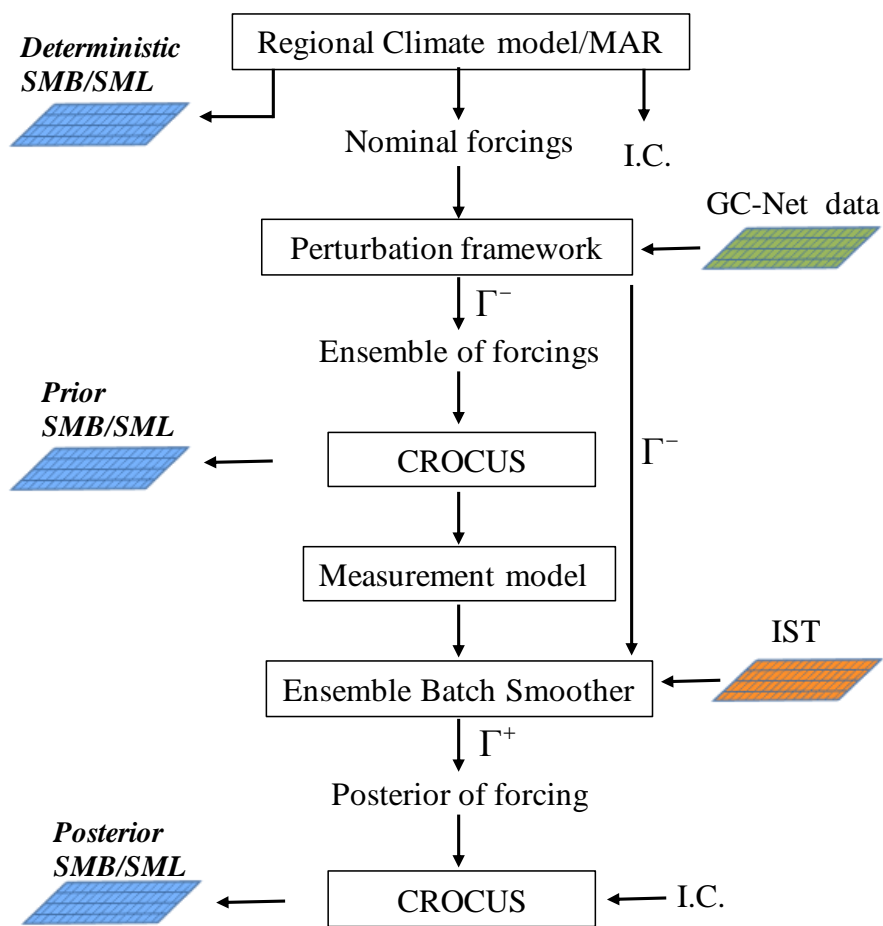
5

6



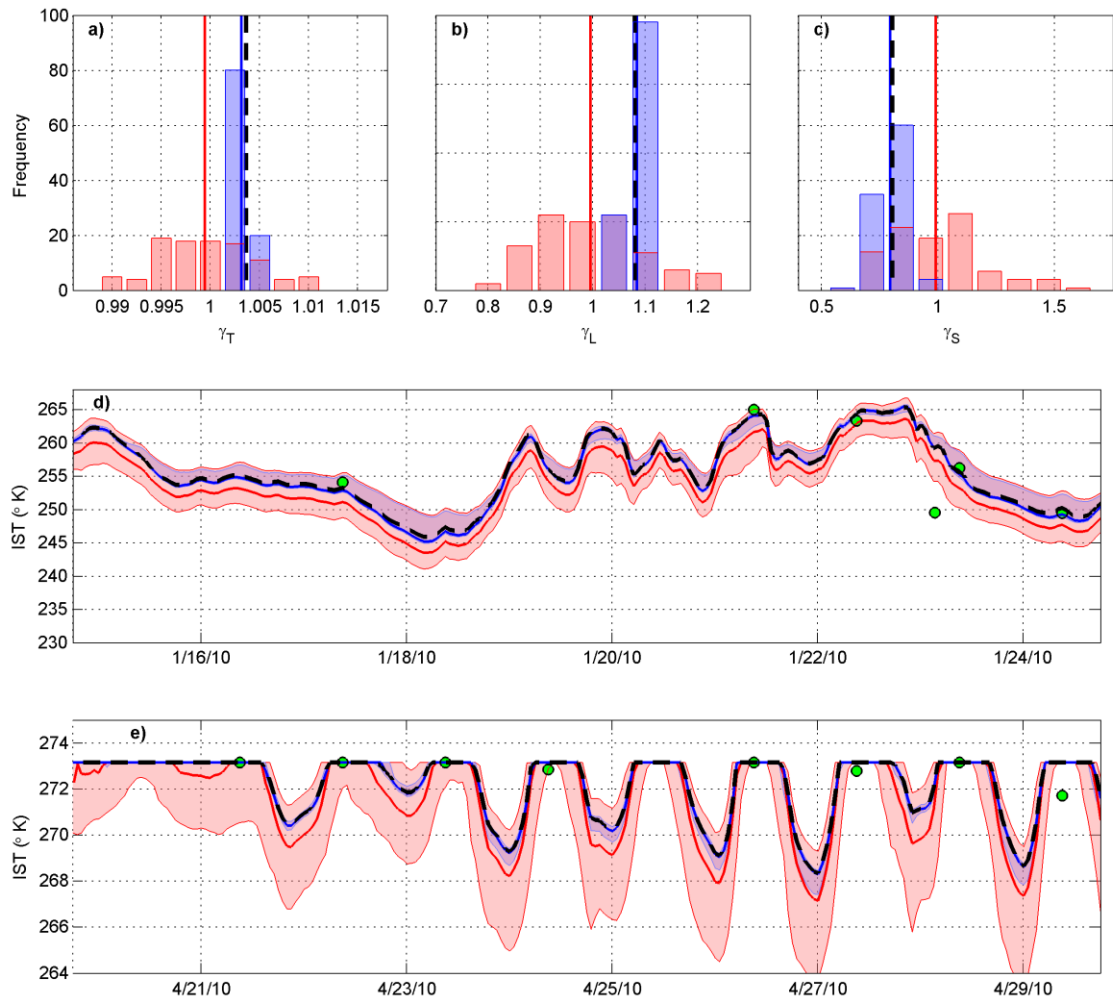
1
2
3
4
5
6
7
8
9
10

Figure 1: The Greenland ice sheet mask (filled area), including the ablation zone (blue), the percolation zone (dark green), and the dry snow zone (bright green) based on an offline CROCUS simulation for the year 2010. The contour lines show the topography of the ice sheet with an interval of 500 m. The red square show the location of pixel in the ablation zone where used to Figure 3



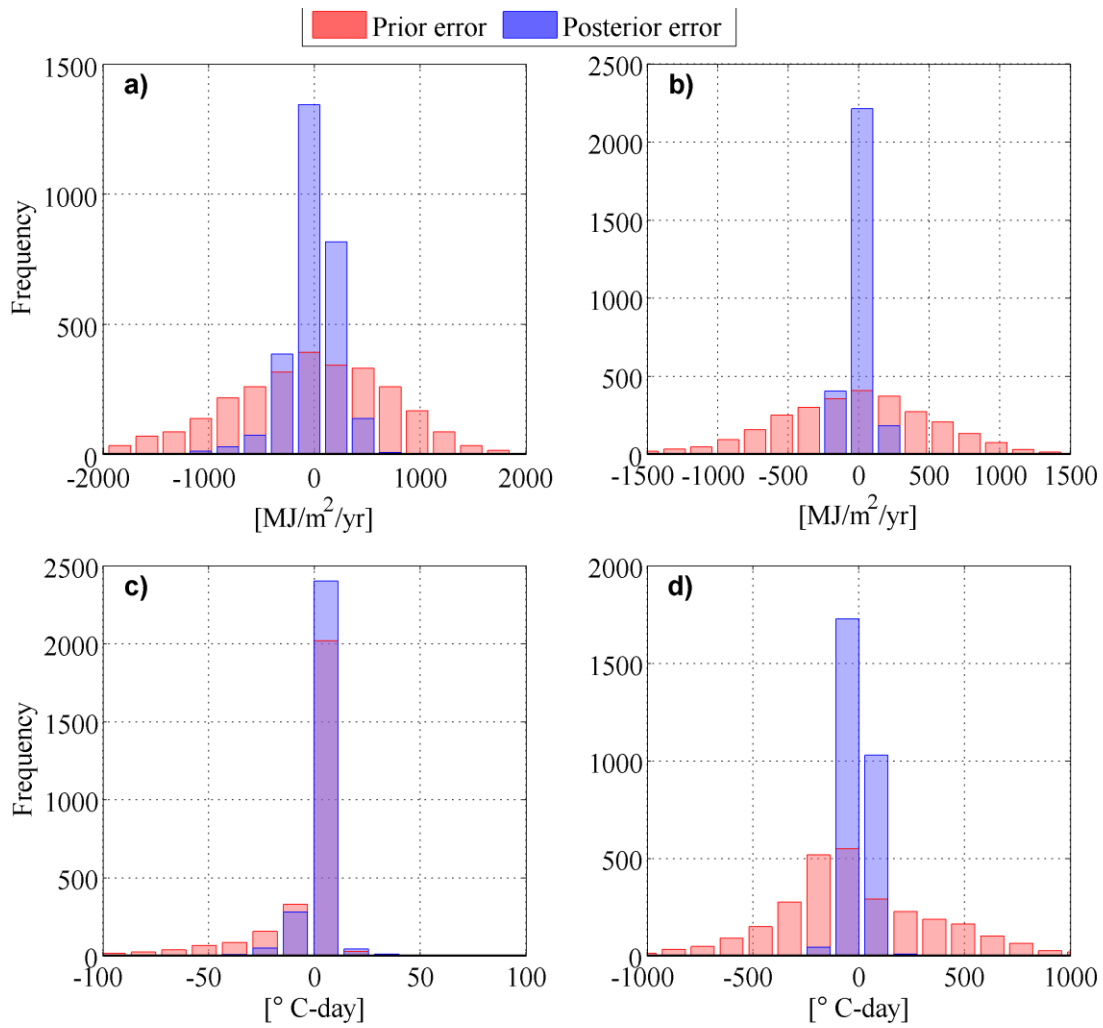
1
2
3
4
5
6

Figure 2: Schematic illustration of the proposed methodology. The posterior SMB/SML is effectively a post-processing (reanalysis) of regional climate model (in this case MAR) estimates conditioned on IST measurements.



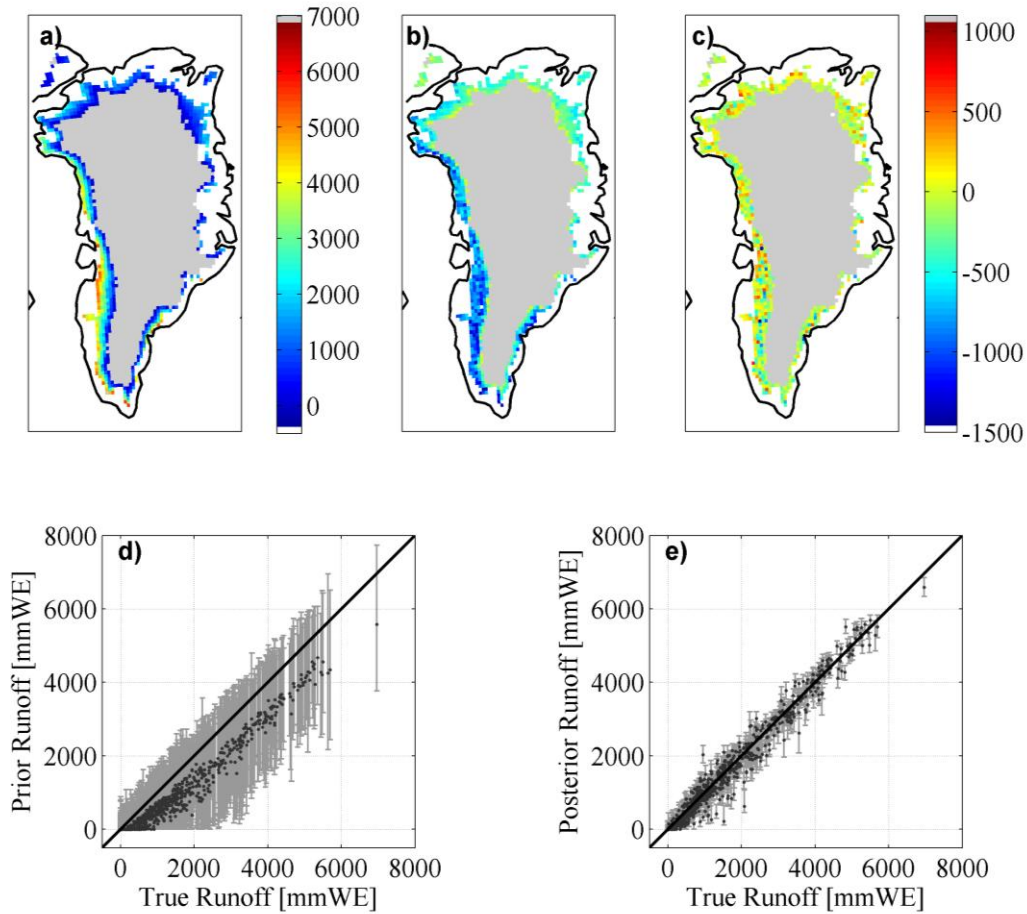
1
2 Figure 3: Ensemble histogram of the prior (red bars) and the posterior (after assimilation of
3 IST) multiplicative states (blue bars) for (a) surface air temperature, (b) longwave radiation,
4 (c) shortwave radiation for a sample pixel in the ablation zone. The prior (red line) and
5 posterior (blue line) median values and truth (black line) are also shown for reference. The
6 time series of: (d) the IST for the 10-day period during the dry season and (e) the IST for the
7 10-day period during the melt season. The red and blue shaded areas represent the prior and
8 posterior uncertainty band (interquartile range) and the red, blue, and black lines represent the
9 median of the prior, the median of the posterior and the truth, respectively. The green circles
10 represent the synthetically generated (noisy) IST measurements that are assimilated to
11 generate the posterior estimates.

12



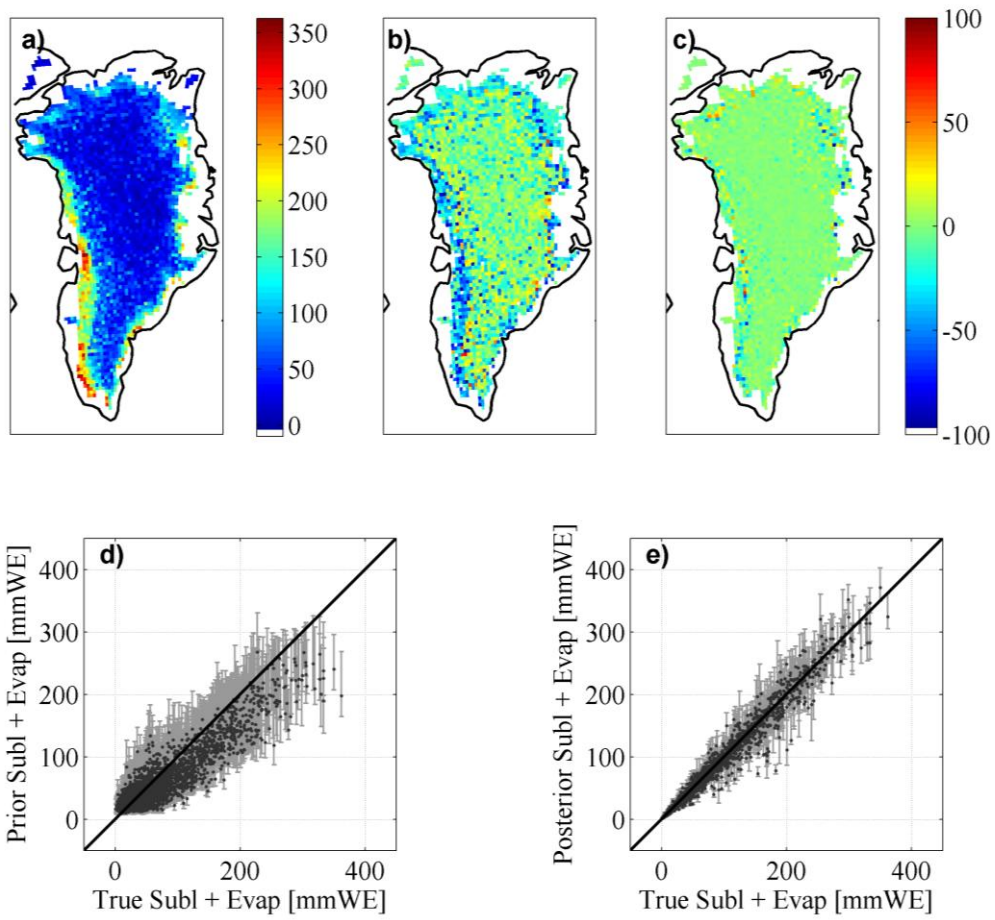
1
2
3
4
5
6
7
8
9
10
11

Figure 4: The histogram of the prior errors (red) and posterior (after assimilation of IST) errors (blue) for cumulative (a) shortwave radiation, (b) longwave radiation, (c) PDD, and (d) NDD over the full GrIS.



1
2
3
4
5
6
7
8
9
10
11
12

Figure 5: The (a) synthetic true runoff (mmWE/yr) for the year 2010, (b) runoff anomaly (mmWE/yr) for the prior (i.e., difference between the prior and true runoff), (c) runoff anomaly (mmWE/yr) for the posterior, (d) scatter plot of the prior runoff estimates, e) scatter plot of the posterior runoff estimates. Black dots are the ensemble median of the estimates and the error bars represent the corresponding ensemble interquartile range of the estimates.



1

2 Figure 6: The same as Figure 5 but for sublimation and evaporation.

3

4

5

6

7

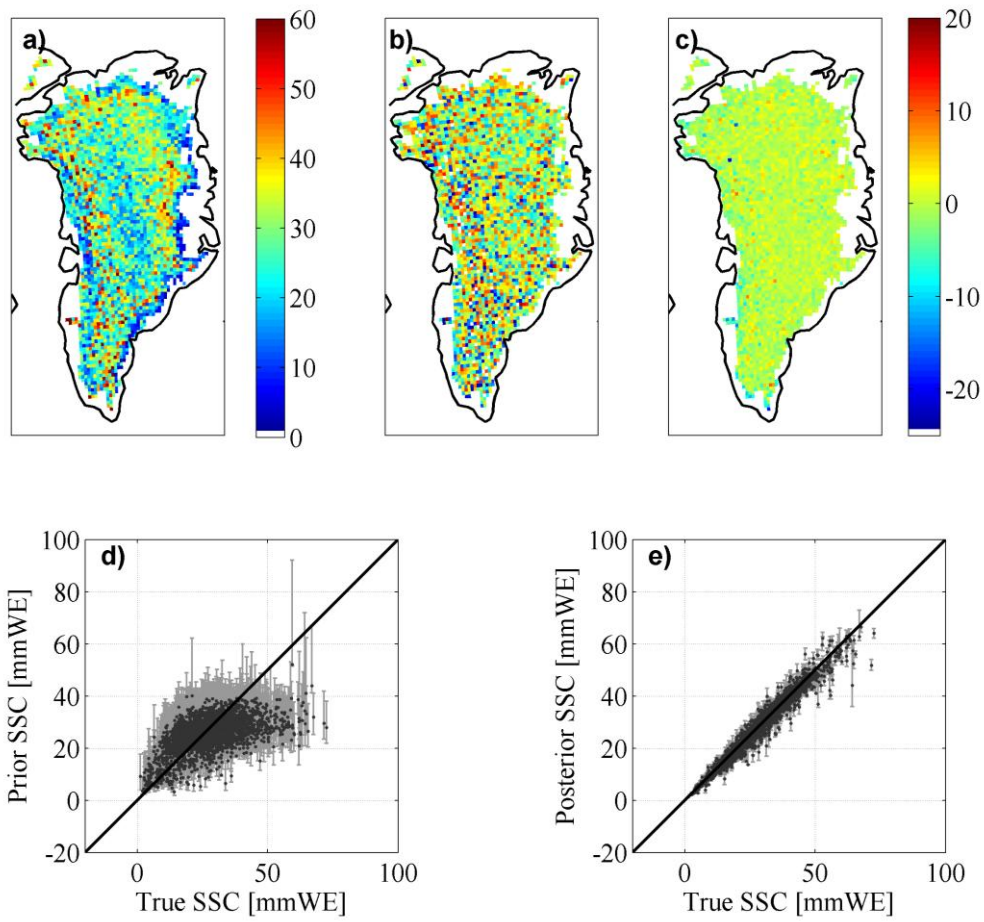
8

9

10

11

12



1

2 Figure 7: The same as Figure 5 but for surface solid condensation (SSC).

3

4

5

6

7

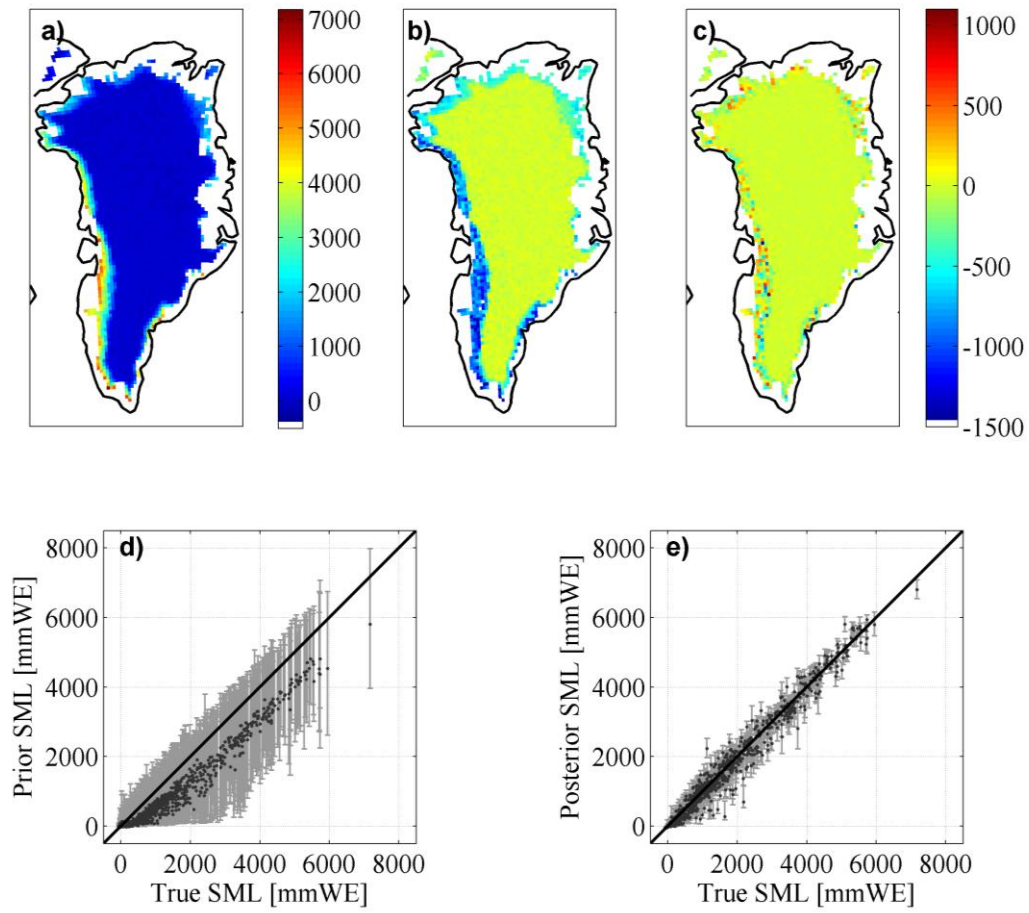
8

9

10

11

12



1

2 Figure 8: The same as Figure 5 but for the GrIS surface mass loss (SML).

3

4

5

6

7

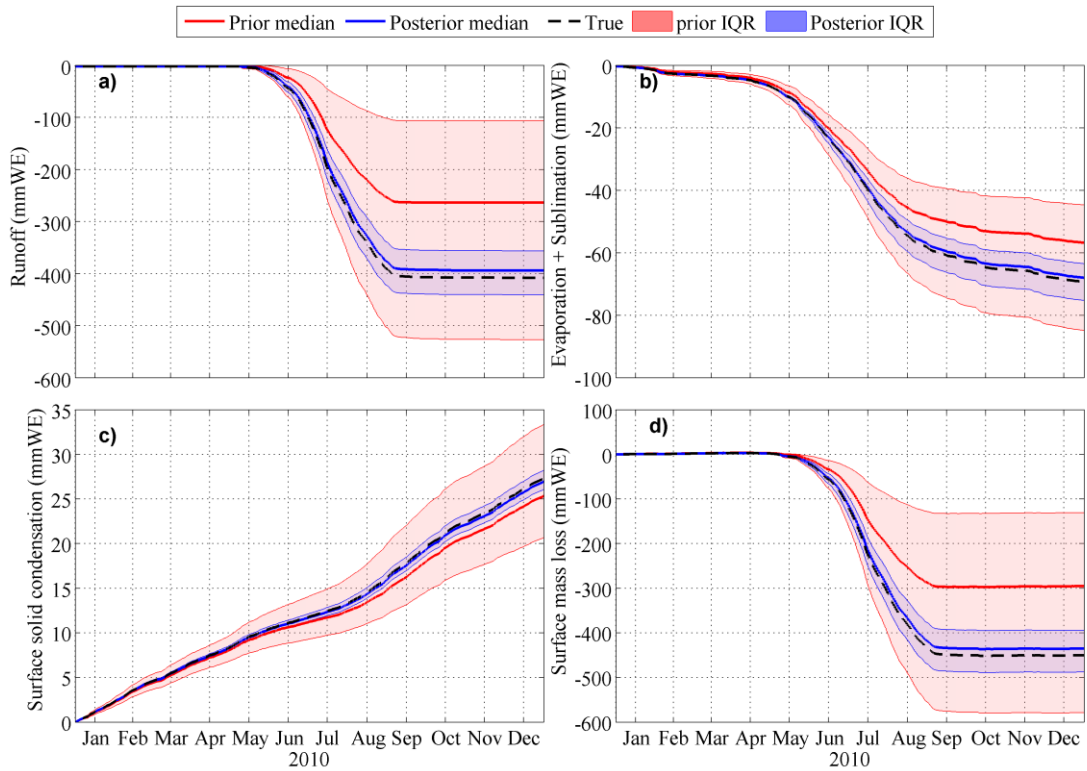
8

9

10

11

12



1

2

3 Figure 9: The time series of: (a) cumulative runoff, (b) cumulative sublimation and
 4 evaporation, (c) cumulative surface solid condensation, and (d) cumulative mass loss over the
 5 GrIS (in millimetres of water equivalent). The truth is the black dashed line, the prior
 6 ensemble median is the red line and the posterior ensemble median is the blue line. The red
 7 shaded area corresponds to the ensemble interquartile range (IQR) for the prior simulation
 8 and the blue shaded area corresponds to the ensemble IQR for the posterior estimates.

9

10